Three-gap superconductivity with T_c above 80 K in hydrogenated 2D monolayer LiBC

Hao-Dong Liu [1,2] Bao-Tian Wang,[3,4] Zhen-Guo Fu [1,*] Hong-Yan Lu [5,†] and Ping Zhang[1,5,‡]

[1]*Institute of Applied Physics and Computational Mathematics and National Key Laboratory of Computational Physics, Beijing 100088, China*

[2]*Graduate School, China Academy of Engineering Physics, Beijing 100088, China*

[3]*Institute of High Energy Physics, Chinese Academy of Sciences, Beijing 100049, China*

[4]*Spallation Neutron Source Science Center, Dongguan 523803, China*

[5]*School of Physics and Physical Engineering, Qufu Normal University, Qufu 273165, China*

(Received 28 February 2024; accepted 29 July 2024; published 3 September 2024)

Although the metallization of semiconductor bulk LiBC has been experimentally achieved, various flaws, including the strong lattice distortion, the uncontrollability of phase transition under pressure, usually appear. In this work, based on the first-principles calculations, we propose a new way of hydrogenation to realize metallization. Using the fully anisotropic Migdal-Eliashberg theory, we investigate the superconducting behaviors in the stable monolayers LiBCH and LiCBH, in which C and B atoms are hydrogenated, respectively. Our findings indicate that the monolayers possess the high T_c of 82.0 and 82.5 K, respectively, along with the interesting three-gap superconducting natures. The Fermi sheets showing the obvious three-region distribution characteristics and the abnormally strong electron-phonon coupling are responsible for the high-T_c three-gap superconductivity. Furthermore, the T_c can be dramatically boosted up to 120.0 K under 3.5% tensile strain. To a great extent, the high T_c is beyond the liquid nitrogen temperature (77 K), which is beneficial for the applications in future experiments. This study not only explores the superconducting properties of the monolayers LiBCH and LiCBH, but also offers practical insights into the search for high-T_c superconductors.

DOI: 10.1103/PhysRevResearch.6.033241

I. INTRODUCTION

The multigap superconductors generally imply the presence of several superconducting gaps that open up on separate and distinct regions of the Fermi surfaces (FSs) [1]. These materials exhibit a competitive and coupled behavior due to multiple condensates, leading to the emergence of various new physical properties [2–6] and theoretical development [7]. However, the limited availability of multigap superconductors poses a significant challenge in confirming these predictions experimentally. This changed after the discovery of the two-gap bulk MgB_2 superconductor [8]. According to Bardeen-Cooper-Schrieffer (BCS) theory [9], MgB_2 exhibits a high superconducting transition temperature (T_c) of ∼40 K [8] due to its high phonon frequency, strong electron-phonon coupling (EPC), and large density of states (DOS) at the Fermi level (E_F). This discovery reignited interest in layered BCS-type compounds that are metallic or can be metallized. Recent discoveries [10–12], especially superconductivity up to 32 K in the pressurized MoB_2 [13], have further fueled this renaissance. It is also worth noting that a strong covalent σ bond above the E_F, consisting of a spin singlet pair with opposite spins [14], is essential for superconductivity. It breaks the binding force of the band, allowing electrons to become itinerant and resulting in strong EPC and a potentially high T_c [14–17]. In the pursuit of identifying novel phonon-mediated superconductors with higher T_c under ambient pressure, several potential candidates have been proposed.

Bulk LiBC [18] has garnered attention for its analogical resemblance and straightforward fabrication. It is isostructural to MgB_2 [19], which effortlessly meets the aforementioned high-T_c criteria. The crystal structure is derived from the fully intercalated graphite structure of MgB_2: Mg → Li and B_2 → BC, resulting in B being the nearest neighbor to C due to the hexagonal arrangement of BC layers. Although the Li atom has one less valence electron than Mg, C possesses one more electron than B. This renders bulk LiBC isovalent with MgB_2 and hugely probable to exhibit metallic properties. Unfortunately, it is a semiconductor with covalent bonding states situated on the top of the valence bands [18,20].

Over the years, extensive efforts have been dedicated to transforming LiBC into a metallic state in order to explore its superconducting properties. Currently, there are several approaches to metallize it. (1) It was theoretically discovered that the injection of Li vacancies ($Li_{0.5}BC$) in bulk LiBC can raise the σ-bonding states above E_F and result in a superconducting state with a T_c of approximately 100 K [21], while a higher concentration of Li vacancies in $Li_{0.125}BC$ was predicted to yield a T_c of up to 65 K [22]. However, with the introduction of Li vacancies, strong lattice distortion follows [23], causing a significant change in the band structure and

*Contact author: fu_zhenguo@iapcm.ac.cn
†Contact author: hylu@qfnu.edu.cn
‡Contact author: zhang_ping@iapcm.ac.cn

TABLE I. First line denotes the number of different bands. The second (fourth) and third (fifth) lines denote the Wannier functions spread of different bands of LiBCH (LiCBH) with (w) and without (w/o) p orbitals of Li atom, respectively.

	Orbital number	1	2	3	4	5	6	7	8	9	10	11	12	Total
w, w/o	w p	1.047	0.976	0.895	0.887	0.791	0.870	0.731	0.724	1.820	2.003	1.726	1.723	14.193
p	w/o p	1.055	1.111	0.904	0.896	0.813	1.126	**100.473**	**99.078**	1.064				**206.520**
Orbitals	w p	1.034	0.949	0.890	0.882	0.791	0.882	0.732	0.726	1.816	2.023	1.736	1.733	14.194
	w/o p	1.042	1.061	0.899	0.891	0.802	**93.613**	0.746	0.739	1.062				**100.855**

weakening the positive effects of lifting the σ-bonding band above the E_F [23]. Consequently, superconductivity has never been observed in synthetic Li_xBC [23–26]. (2) To suppress the impact of introducing the lattice distortion and simultaneously metallizing LiBC-type compounds, Miao [27] and Gao [14] *et al*. proposed an idea of partial substitution between C and B atoms. Investigations have demonstrated that certain LiBC-type compounds, such as $LiB_{1.1}C_{0.9}$ [27], $Li_3B_4C_2$ [14], $LiBC_3$ [28], and $Li_4B_5C_3$ [29], exhibit superconductivity with T_c values of 36, 50, and 16.8 K, respectively. However, the synthesis of these B-enriched stoichiometric compounds has proven to be challenging [30]. Additionally, the hole-doped $Li_xB_{1.15}C_{0.85}$ exhibits a significant decrease in resistivity below 20 K but does not exhibit superconductivity [31]. (3) Another possible way to realize the metallization is by applying pressure. However, Lazicki *et al.* found that, even at 60 GPa [32], the crystal structure of LiBC remains unaltered. Subsequently, the theoretically calculated pressure required for its metallization is up to 345 GPa. However, pressure also eliminates the similarity of electronic structure between LiBC and MgB_2 [32,33], resulting in a new phase. (4) Dimensional reduction is a significant route to achieving metallization of bulk LiBC. Gao and Modak *et al*. have investigated the effects of dimensional reduction on metallization, leading to superconductivity with T_c of ∼90 K in trilayers LiB_2C_2 [34] and 70 K monolayer LiBC [35], respectively. This method seems to be a viable way to explore the superconductivity of the LiBC compound, but experimental verification is imperative.

Is there another possible approach to realizing the metallization of LiBC? Here, one initial idea that comes to our mind is to explore hydrogenation as a means to achieve it. Dense metallic hydrogen [36] can lead to a high-temperature superconductor with T_c of 242 K [37] under ultrahigh pressure (∼400 GPa) [38,39], accompanied by multigap superconducting characteristics [37]. Over the years, hydrogenation, as an active way to boost the T_c of superconductors, has been widely studied [40–47]. Thus the idea to achieve the metallization of the LiBC compound is hydrogenation. First, monolayer LiBC can be exfoliated from the bulk LiBC [18] to realize dimensional reduction. Subsequently, the H atom can be added to the side of the Li layer for realizing its hydrogenation. In this work, presenting the common advantages of dimensional reduction [34,35,48,49] and hydrogenation [36,37], LiBCH and LiCBH are predicted to be high-T_c superconductors.

II. COMPUTATIONAL METHODS

In these DFT calculations, the subsequent lattice optimization, dynamic matrices, and electronic and phononic calculations were performed by using the QUANTUM ESPRESSO (QE) package [50] with the projector augmented wave (PAW) [51–53]. The exchange-correlation potentials were described by the generalized-gradient approximation (GGA) functional of the Perdew-Burke-Ernzerhof (PBE) [54] formula. 100 and 800 Ry were chosen to be the kinetic energy cutoff and charge density cutoff of the plane wave basis, respectively. A sufficient vacuum space of 20 Å was added to the models to eliminate the periodic interaction between adjacent layers. The charge densities were calculated on an unshifted k mesh of $48 \times 48 \times 1$ points in combination with a Methfessel-Paxton smearing [55] of 0.02 Ry. The convergence criteria for energy and force were set as 10^{-7} and 10^{-6} Ry a.u.$^{-1}$, respectively. The dynamical matrices and the perturbation potentials were calculated on a Γ-centered $12 \times 12 \times 1$ mesh, within the framework of density-functional perturbation theory [56]. The aforementioned parameters were selected after the full convergence tests. The lattice constants after full relaxation were also adopted.

We further used a method of Wannier interpolation function to reevaluate the EPC of monolayers LiBCH and LiCBH. A $12 \times 12 \times 1$ grid was used to construct the maximally localized Wannier functions (MLWFs) [57–59] in the BZ, to perform the precedent non-self-consistent calculations of the electronic wave functions. We chose 12 electron orbitals to fully describe the band structures (Fig. 7) around the E_F. To be more precise, eleven are the s, p orbitals of boron, carbon, and p orbitals of lithium atom; the last one is the s orbital of the H atom (s orbital of Li can be neglected [35]). The values of each spatial spread are smaller than that of the lattice constant, presenting excellent localization in real space. Meanwhile, to validate the necessity of Li atomic p orbitals in the construction of tight-binding models, we also listed the spatial spread with and without Li atomic p orbitals (Table I). Based on the EPW code [60–62], the convergence analysis of EPC constant λ was tested by an electron and a phonon mesh consisting of $200 \times 200 \times 1$ and $100 \times 100 \times 1$ points, respectively. More computational details are presented in Appendix A.

III. RESULTS AND DISCUSSIONS

A. Crystal structures

The starting point is to ascertain the equilibrium structure of the hydrogenated LiBC system. To achieve this goal and eliminate the influence of different H atomic concentrations, we examine several potential high-symmetry sites shown in Fig. 1(c) and simulate the corresponding dynamic stabilities. As detailed in Fig. 6, only two dynamically stable structures with one H adatom per unit cell are observed. Their sufficiently optimized structures are distinguished by H sites

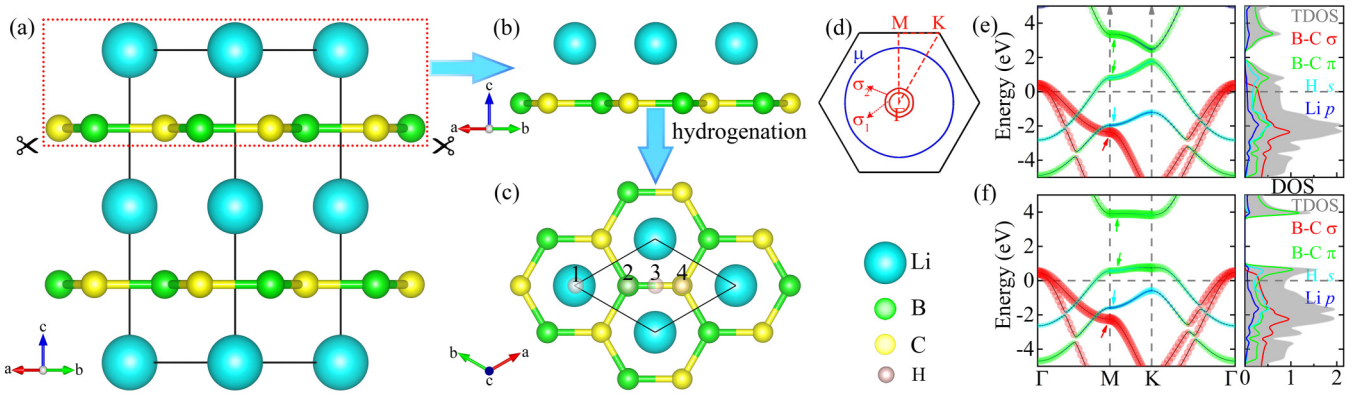

FIG. 1. Optimized geometries of (a) bulk LiBC, (b) the exfoliated monolayer LiBC, and (c) the top view of hydrogenated monolayers LiBC with different hydrogenating sites, where the "1, 2, 3, 4" represent the H adatoms located at the top of Li, B, center of B-C bonds, and C atoms, respectively. The unit cell comprising four atoms is marked as a rhombus. (d) Fermi surface of LiBCH and LiCBH. The red and blue curves represent the Fermi sheets originated from the B-C σ states (the inner and outer named as σ_1 and σ_2, respectively) and hybridized states of B π and H s orbitals (named as μ), respectively. The high symmetric route along Γ-M-K-Γ is shown in red dotted lines. Panels (e) and (f) represent the electronic properties of monolayers LiBCH and LiCBH, respectively.

in which B and C are hydrogenated, named as LiBCH and LiCBH, respectively. The total energy per atom of LiBCH is lower by about 20 meV than that of LiCBH. The calculated crystal parameters can be obtained in Table II. Moreover, stability is important for a new material. Thus we prove their thermodynamic, mechanical, dynamic, and electronic stability, where the details are provided in Appendix E.

B. Electronic and phononic properties

Based on the overall analysis in Appendix H, we can draw the following conclusion about charge transfer: Li-s and C/B-p_z orbitals lose charges; Li-p, C/B-p_x, p_y, and H-s orbitals get charges. On the whole, C/H and B/Li atoms obtain and lose charges, respectively. The band structures and DOS for LiBCH and LiCBH are shown in Figs. 1(e) and 1(f). The orbitals with little contributions at the E_F, such as the s orbitals of B(C), are omitted. There are three bands across the E_F—one band along the high-symmetry points M and K is mainly composed of the hybridized states of B/C-π and H-s orbitals and two bands around the BZ center originate from the B/C-σ states, leading to two hole pockets. It is indicative of metallization motivated by covalent states, analogous to what is observed in other multigap superconductors MgB_4 [63], AlB_2-based films [64], and MgB_2 [16,29,65,66]. Moreover, the band gaps between the valence band maximum (VBM) and conduction band minimum (CBM) of LiBCH and LiCBH around K point are 0.722 and 3.073 eV, respectively. As depicted in the DOS, the dominant electronic states near the E_F come from the contribution of B/C-σ, -π, and H-s orbitals, with minor contribution from Li-p orbitals. Hence, compared with those electrons of LiBC only from B/C-σ and -π states [35], hydrogenation can bring higher electronic DOS at the E_F, which benefits EPC. However, Li-p orbitals play essential roles in the construction of more localized Wannier functions, as shown in Fig. 7 and Table I. The constraint of the B-C lattice subjects the Li atom to substantial lattice chemical pressure with energetic level transitions from the 1s to 2p orbitals. This feature is not unique and has also been reported in monolayer LiBC [35]. The van Hove singularities are indicated by colored arrows, with each color representing a different dominant orbital. Figure 12 shows the projections of Fermi velocity and different orbitals on the FSs of LiBCH and the corresponding FSs of LiCBH are shown in Fig. 13. Here, as an example, we are focused on the properties of LiBCH. Just as mentioned earlier, from Γ point to the BZ boundary, there are three regularly circular Fermi sheets. In detail, the two inner are formed by the B/C-σ states (marked as the σ_1 and σ_2, respectively) and the outer sheet originates from the hybridized states, named the μ, of B/C-π and H-s orbitals. The emergence of different component sheets (σ_1, σ_2, and μ sheets) signifies that the LiBCH and LiCBH can become candidates of multigap superconductors. Moreover, it is clearly observed that some anisotropic distributions, such as Fermi velocity, p_x and p_y orbitals of B/C, and so on, exist in some sheets, whether the inner or outer. Therefore, the observed behaviors on the FSs prompt us to employ the anisotropic Migdal-Eliashberg theory [62,67–70] to solve the EPC of LiBCH and LiCBH.

Based on the absence of negative frequencies, the phonon dispersion indicates that the system is positioned at the lowest point in its energy landscape and possesses dynamic stability

TABLE II. Fully optimized lattice parameters a, the bond lengths of C-B and Li-H, and the perpendicular distance of C-B Δh_1, Li-H Δh_2, and C-Li h in Å for LiBCH and LiCBH.

	Parameters	a	C-B	Li-H	Δh_1	Δh_2	h
Materials	LiBCH	2.7258	1.5751	1.7429	0.0659	0.7490	1.7893
	LiCBH	2.7255	1.5736	1.7325	0.0058	0.7249	1.9048

(Fig. 9). There are four atoms in the primitive cell, which results in twelve phonon modes: three acoustic and nine optical branches. Moreover, with no regard to the acoustic modes and the analysis of the C_{3v} point group, the nine optical phonon modes at the Γ point can be disassembled as

$$\Gamma_{\text{optical}} = 3E(I+R) + 3A_1(I+R), \quad (1)$$

where I and R represent the Raman and infrared modes. Table VI presents further details on the vibration modes observed at the Γ point, including their symmetry, vibrational properties, Raman/infrared activity, and frequencies, which will aid in guiding future experimental works. The phonon dispersions weighted with atomic vibrational directions and the projected phonon density of state (PhDOS) over the whole frequency are described in Fig. 14. As a result of the similarity in structure, the distributions of atomic vibration for LiBCH and LiCBH bear a close resemblance to each other. Meanwhile, owing to the slight disparities in atomic mass, there is a lack of clear demarcations in the vibrational distributions of different atoms. Simply, the vibrational distributions of B and C atoms span the entire frequency range, with the predominant focusing on medium and high frequencies (above 35 meV). Meanwhile, the distributions of H atoms are bifurcated, with one portion predominating in high frequencies (above 75 meV) and the other portion residing in low frequencies (below 50 meV). Distinctly demarcating, the vibrations of Li atoms emerge within the range of low frequencies below 50 meV. In short, the low below 25 meV mainly originates from the vibrations of Li and H; the medium at the range from 25 to 75 meV is from the vibrations of B/C atoms; the high from 75 to 135 meV is dominated by the vibrations of H and in-plane B/C atoms. Here, the frequencies of optical modes associated with the vibrations of H atoms are close to those (75–127 meV) of the hydrogenated MgB_2 [40] monolayer. It implies that the T_c of our predicted LiBCH and LiCBH may be close to or even higher than that (67 K) of the hydrogenated MgB_2 monolayer.

C. Three-gaps superconductivity

Subsequently, we concentrate on the superconductivity of LiBCH and LiCBH. The related superconducting properties are shown in Figs. 2 and 15 for LiBCH and LiCBH, respectively. As shown in Fig. 2(a), the strong projections of EPC parameters $\lambda_{\mathbf{q}}^{ph}$ are located in two regions: one is the acoustic phonon modes around the Γ point; the other is the BZ-center optical E modes originating from the in-plane (seen in Table VI and Figs. 14 and 16) B-C stretching. The strong coupling between the B/C-σ states and the in-plane phonon vibration of B-C graphenelike net results in the large $\lambda_{\mathbf{q}\nu}^{ph}$ [Fig. 2(b)] around the Γ point and leads to some high peaks of Eliashberg functions $\alpha^2F(\omega)$, particularly the maximum at the optical E modes points. The anomalously large EPC strengths of $\lambda_{\mathbf{q}\nu}^{ph}$ are from the dramatic softening of the optical E modes with the existence of Kohn anomaly [71], rather than the effect of nesting function shown in Fig. 10. There is a strong concordance between the regions where optical phonons experience softening in the BZ and the diameter of hole Fermi sheets that arise from the σ-bonding B/C orbitals, demonstrating a typical attribute associated with the Kohn

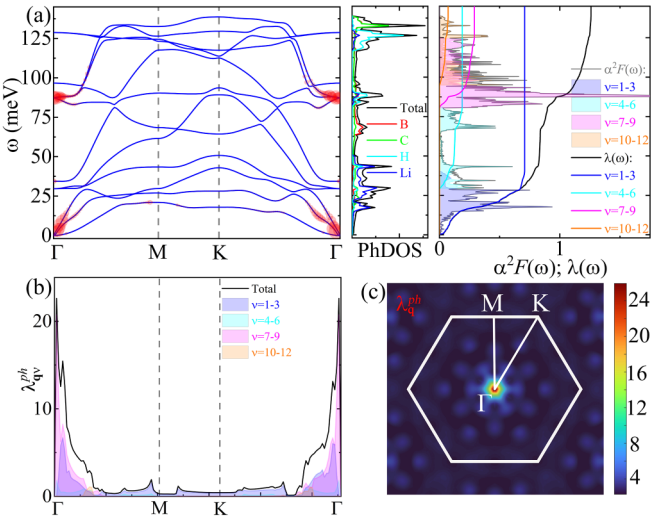

FIG. 2. Properties of lattice dynamics and EPC parameters $\lambda_{\mathbf{q}}^{ph}$ for the LiBCH monolayer. (a) Phonon weighted with the EPC parameters $\lambda_{\mathbf{q}}^{ph}$ (red), PhDOS, and the total cumulative EPC $\lambda(\omega) = 2\int \alpha^2F(\omega)/\omega\, d\omega$ with the corresponding mode-resolved Eliashberg spectral function $\alpha^2F(\omega)$. (b) EPC $\lambda_{\mathbf{q}\nu}^{ph}$ along the high-symmetry line Γ-M-K-Γ. (c) EPC $\lambda_{\mathbf{q}}^{ph}$ projected in the whole BZ.

effect [63,72]. These findings are further corroborated by the mode-resolved $\alpha^2F(\omega)$ and $\lambda(\omega)$. Moreover, for LiBCH (LiCBH), the three low-frequency acoustic phonon branches $\nu = 1$–3 contribute 56.3 (62.5)% of the total EPC $\lambda(\omega)$, while the remaining modes $\nu = 4$–6, 7–9, and 10–12 contribute 15.0 (15.0)%, 23.0 (18.6)%, and 5.7 (3.9)%, respectively. The total EPC λ is up to 1.26 (1.36).

The EPC parameters $\lambda_{\mathbf{k}}^{el}$ on the FS and strength distribution $\rho(\lambda_{\mathbf{k}}^{ph})$ are shown in Fig. 3. The detailed discussion about the differences and correlations can be obtained in Ref. [73]. For LiBCH (LiCBH), the range of the whole EPC $\lambda_{\mathbf{k}}^{el}$ is from 0.87 (0.85) to 2.31 (2.63). The latter is slightly larger than that of the former. Moreover, the larger EPC $\lambda_{\mathbf{k}}^{el}$ exhibits in the σ_1 and σ_2 sheets, while the μ sheet possesses the smaller value of $\lambda_{\mathbf{k}}^{el}$. The strength distributions of σ_1, σ_2, and μ, namely $\rho(\lambda_{\mathbf{k}}^{el,\sigma_1})$, $\rho(\lambda_{\mathbf{k}}^{el,\sigma_2})$, and $\rho(\lambda_{\mathbf{k}}^{el,\mu})$, are from 1.98 (2.27), 1.47 (1.67), and 0.87 (0.85) to 2.31 (2.63), 1.92 (2.14), and 1.07 (1.18), respectively. The resulting average of EPC λ^{el} is 1.69

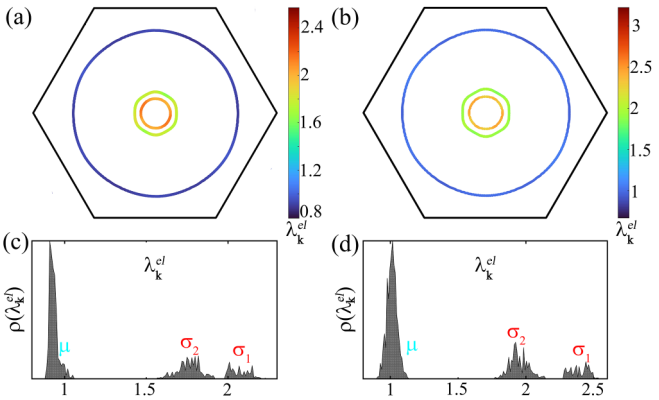

FIG. 3. EPC parameters $\lambda_{\mathbf{k}}^{el}$ and strength distribution $\rho(\lambda_{\mathbf{k}}^{el})$ for (a), (c) LiBCH and (b), (d) LiCBH, respectively.

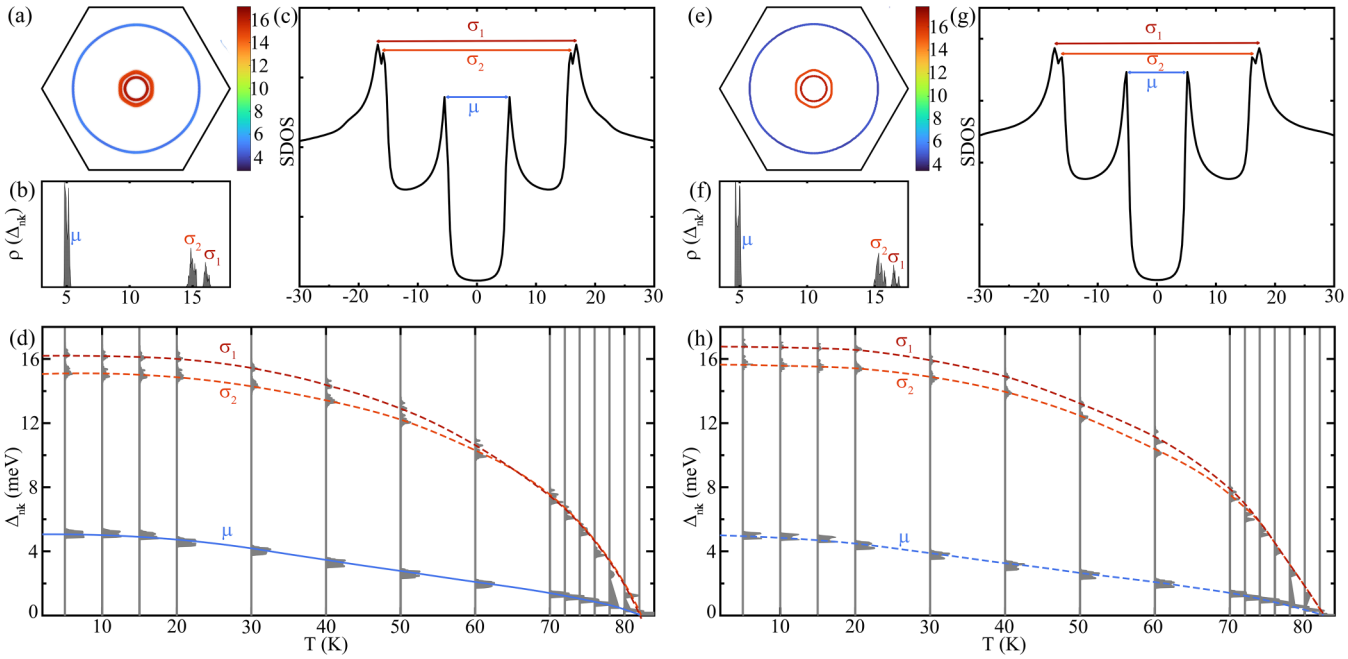

FIG. 4. Superconducting gap properties of LiBCH and LiCBH. (a) Momentum-resolved superconducting gap $\Delta_{n\mathbf{k}}(\omega = 0)$ on the FS at $T = 5$ K; (b) the strength distributions of gaps $\rho(\Delta_{n\mathbf{k}})$; (c) SDOS at $T = 5$ K; (d) energy distribution of the gaps $\Delta_{n\mathbf{k}}$ versus T for LiBCH. (e)–(h) The corresponding superconducting gaps' results for LiCBH. The dark red, red, and blue lines in (d) and (h) are the eye guides for the gaps Δ_{σ_1}, Δ_{σ_2}, and Δ_μ, respectively. [Note: the heights of the histograms are multiplied by a factor of 2.5 while plotting for visibility in (d) and (h)].

(1.82). According to the aforementioned analysis, we can find that the high-frequency optical phonon of the dramatic softening around the Γ point, e.g., the E modes, and the acoustic phonon significantly contribute to forming the large electronic EPC $\lambda_{\mathbf{k}}^{el}$ on the σ_1 and σ_2 sheets.

Meanwhile, the different regions with different electronic states on the FS can lead to the separation of strength distributions ($\lambda_{\mathbf{k}}^{el}$) between the σ and μ sheets. As demonstrated in Figs. 3(c) and 3(d), the behavior that σ sheets are divided into σ_1 and σ_2 sheets results in the formation of three-region strength distribution characteristics of $\lambda_{\mathbf{k}}^{el}$. The reason for separation between the strength distributions can be attributed to the extra slight distribution of the phonon EPC $\lambda_{\mathbf{q}}^{ph}$, e.g., between Γ and K points with a proximity bias towards the Γ point, shown in Figs. 2(c) and 15(c). These slight distributions of $\lambda_{\mathbf{q}}^{ph}$ originate from the weak phononic softening located around the Γ point, shown in Figs. 2(a) and 15(a). The same results have also been observed in MgB_4 [63] and AlB_4 [64].

Based on fully anisotropic Migdal-Eliashberg theory [62,67–70], we now turn to analyzing the superconducting gaps, shown in Fig. 4. Combining with Fig. 3, it is worth noting that the regions with larger gaps on FSs shown in Figs. 4(a) and 4(e) coincide with those with stronger EPC $\lambda_{\mathbf{k}}^{el}$, with the strongest gap Δ_{σ_1}, secondary gap Δ_{σ_2}, and hybridized-states-included weakest gap Δ_μ opening on the σ_1, σ_2, and μ sheets, respectively. The superconducting DOS (SDOS) can be calculated with the formula (24). As shown in Figs. 4(c) and 4(g), the SDOS with three distinguished peaks corresponding to the Δ_{σ_1}, Δ_{σ_2}, and Δ_μ further demonstrates the nature of three superconducting gaps. For LiBCH (LiCBH) at the temperature $T = 5$ K, shown in Figs. 4(b) and 4(f), the ranges of three gaps Δ_{σ_1}, Δ_{σ_2}, and Δ_μ are 15.75 (16.20) ∼16.65 (17.10), 14.46 (14.91) ∼15.36 (15.87), and 4.80 (4.68) ∼5.40 (5.19) meV, respectively. The largest and smallest gap divisions originating from the Δ_{σ_2}, Δ_μ and Δ_{σ_2}, Δ_{σ_1} are 9.06 (9.72) and 0.39 (0.33) meV, respectively. These results agree well with three-region distribution characteristics of electronic EPC $\lambda_{\mathbf{k}}^{el}$, indicating that LiBCH and LiCBH are evidently three-gap superconductors. As depicted in Figs. 4(d) and 4(h), the typical BCS-type temperature dependence occurs due to the changes in gaps $\Delta_{n\mathbf{k}}$ versus T. Moreover, the value of Δ_μ is enlarged from ∼2.7 meV of LiBC [35] to ∼5 meV by introducing the hydrogen. As the temperature increases, the values of $\Delta_{n\mathbf{k}}$ gradually vanish and converge at 82.0 and 82.5 K for LiBCH and LiCBH, respectively. Their T_c are higher than 17–47 K of AlB_{2+x} films [64], 52 K of MgB_4 [63], 53 K of MgB_2 with the strain of 4.5% [48], 67 K of hydrogenated MgB_2 [40], and the pristine T_c of the carbon-cage network [74]. It is interesting that both T_c are beyond the liquid nitrogen temperature (77 K), which are highly significant and evidently beneficial for application in future experiments.

Here, we draw a short discussion about superconducting parameters calculated by the Allen-Dynes (AD) formula. For LiBCH (LiCBH), the results suggest that the EPC λ_{AD} and T_c are 1.19 (1.33) and 36.71 (32.71) K, respectively, about 55.2 (60.4)% less than the values analyzed from the multiband theory. This clearly substantiates that the presence of multigaps, three gaps, here plays a crucial role in capturing the rising T_c.

D. Boost of T_c: Effect of biaxial strain

Due to the significant enhancement of superconductivity under the biaxial strain in numerous 2D materials, e.g., hydrogenated MgB_2 [40], monolayer MgB_2 [48], and

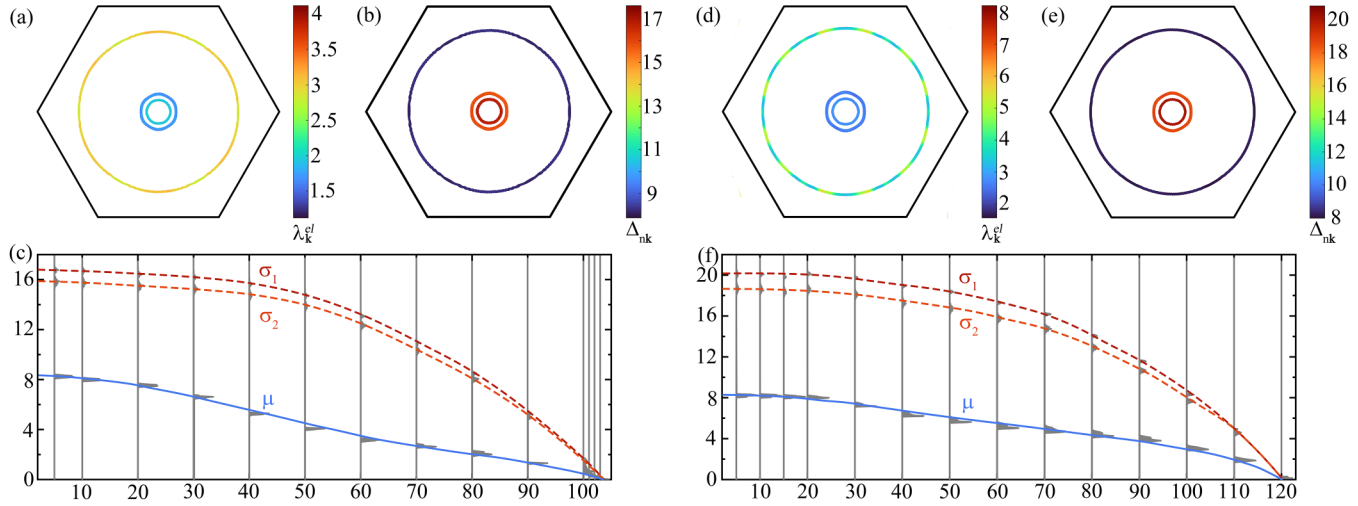

FIG. 5. Superconducting properties of LiBCH and LiCBH under strains. (a) The electronic EPC parameters $\lambda_{\mathbf{k}}^{el}$; (b) momentum-resolved superconducting gap $\Delta_{n\mathbf{k}}(\omega = 0)$ on the FS at $T = 5$ K; (c) energy distribution of the gaps $\Delta_{n\mathbf{k}}$ versus T for LiBCH at the $\varepsilon = 2.1\%$ strain. (d)–(f) The corresponding superconducting results for LiCBH at the $\varepsilon = 3.5\%$ strain. The dark red, red, and blue lines in (c) and (f) are the eye guides for the gaps Δ_{σ_1}, Δ_{σ_2}, and Δ_{μ}, respectively.

hole-doped graphene [75,76], its effect on the superconductivity of LiBCH and LiCBH should also be explored. We gradually impose the biaxial stretching strains (ε) effect until the appearance of obvious imaginary frequencies. For LiBCH (LiCBH), shown in Fig. 17, the results suggest that they can possess dynamical stability unless the strain exceeds $\varepsilon = 2.1$ (3.5)%. Furthermore, when the phonon softening in LiBCH and LiCBH is magnified by modulation until prominent imaginary frequencies (solid red lines of Fig. 17) emerge, it becomes vulnerable to a charge density wave (CDW) transition. This means that the optimized structures are the dynamically stable superconductors, but are closed to the CDW states. Next, preceding the appearance of CDW transition, our calculations indicate that the strains can sufficiently boost the T_c and other superconducting parameters.

The calculated EPC parameters $\lambda_{\mathbf{q}}^{ph}$ projected on the phonon spectra and BZ, as well as the Eliashberg function $\alpha^2F(\omega)$, are shown in Fig. 18. We find that the dramatical softening modes appear around 1/3 K-Γ, where some large EPC parameters $\lambda_{\mathbf{q}}^{ph}$ accumulate, shown in Figs. 18(a) and 18(d). Meanwhile, as depicted in Figs. 18(b), 18(c), 18(e), and 18(f), one visible peak of $\lambda_{\mathbf{q}}^{ph}$ also emerges around 1/3 K-Γ. Furthermore, some high peaks of $\alpha^2F(w)$ are triggered, forming a large λ from the formula $\lambda = 2\int_{\mathbf{q}_{v=3}}^{\mathbf{q}_{v=1}} \alpha^2F(w)\omega^{-1}d\omega$. Combining with Figs. 14(j) and 14(n), the out-of-plane vibration of H atoms plays an essential role in the large EPC and formation of strong softening modes, meaning that H atoms can significantly enhance the EPC. Notably, around this $\mathbf{q}$ point, there is a certain degree of improvement in the effect of nesting function, shown in Figs. 10(f) and 10(h). More importantly, the EPC constants λ for LiBCH and LiCBH are sharply boosted up to 2.54 and 3.45, respectively, which lead them to become strong EPC superconductors. A larger portion of the EPC constant λ in LiCBH compared to LiBCH can be traced back to the anomalous concentration of EPC $\lambda_{\mathbf{q}}^{ph}$ around 1/3 K-Γ, shown in Figs. 18(b) and 18(e).

The other superconducting parameters, e.g., superconducting gaps, EPC $\lambda_{\mathbf{k}}^{el}$ on the FS, are centrally exhibited in Fig. 5. As shown in Figs. 5(a) and 5(d), the regions with lager $\lambda_{\mathbf{k}}^{el}$ on the FS appear in the μ sheets, rather than the σ sheets of equilibrium cases ($\varepsilon = 0\%$). This demonstrates again the important effects of H atoms on the boost of superconductivity. The retention of characteristics of three-gap superconductivity in the monolayers LiBCH and LiCBH is due to the almost consistent FS with the equilibrium cases, as shown in Figs. 5(b) and 5(e). The large superconducting gaps still open on the σ_1 and σ_2 sheets, which are much larger than the equilibrium cases. Last but not least, the superconductivity transition temperatures T_c for the LiBCH and LiCBH are sharply boosted up to 103.5 and 120.0 K, respectively. It is incredibly interesting that these predicted high T_c beyond 100 K at ambient pressure are rare in the current research of 2D superconductors, which is of high significance and broad prospect.

E. Discussion

Before drawing a conclusion, it is extremely worth noting that this research represents a direction for searching high-T_c superconductors at ambient pressure, taking full advantage of the following aspects: the nature of multigaps, the σ bonds of B-C graphene-like net, and H atoms. The multigaps can possibly open larger superconducting gaps, resulting in the higher T_c [63,77,78]. The σ bonds of B-C graphenelike net usually provides stronger EPC parameters $\lambda_{\mathbf{q}}^{ph}$ which can trigger higher peaks of $\alpha^2F(\omega)$ and subsequently stronger EPC [79]. The advantages of H atoms can raise the upper limit of phonon frequency ω and boost the value of T_c, especially in the strain engineering. In addition, dimensional reduction can also effectively increase T_c [48,49]. Based on these principles, we believe that more superconductors with higher T_c can be discovered.

IV. CONCLUSIONS

In summary, we find two stable hydrogenated LiBC configurations from $LiBCH_x (x = 1, 2, 3, 4)$ with different H atomic concentrations. Subsequently, their stabilities, charge transfer, and electronic/phononic properties are studied. By solving the fully anisotropic Migdal-Eliashberg equations, superconducting behaviors are investigated systematically. We observe an interesting nature of three-gap superconductivity with high T_c of 82.0 and 82.5 K and reveal that the strong electronic EPC parameters $\lambda_{\mathbf{k}}^{el}$ with evident three-region distribution characteristics are responsible for this high-T_c three-gap superconductivity. Moreover, our calculations suggest that the dominating phononic EPC parameters $\lambda_{\mathbf{q}}^{ph}$, resulting from the acoustic and high-energy optical softening phonon modes around the BZ center, contribute to larger $\lambda_{\mathbf{k}}^{el}$ between the σ_1 and σ_2 Fermi sheets. The distinct separation of the σ sheets further indicates the formation of three-region distribution characteristics of $\lambda_{\mathbf{k}}^{el}$ and the robust three-gap superconducting behaviors. We also discover that the coupling between the covalent metallized states and in-plane phonon vibration modes originating from the B-C graphenelike net play an essential role in superconductivity. In addition, the T_c can be dramatically boosted up to 103.5 and 120.0 K under the small strains $\varepsilon = 2.1\%$ and 3.5%, respectively. The large boost of T_c originates from the H atomic out-of-plane phononic vibrations on the outer μ sheet, rather than the inter-σ sheets in the pristine cases. This work not only explores the superconducting properties of the LiBCH and LiCBH monolayers but also provides practical insights into the search for high-T_c superconductors.

ACKNOWLEDGMENTS

This work was supported by the National Natural Science Foundation of China (Grants No. 12175023, No. 12074213, and No. 11574108), the Major Basic Program of Natural Science Foundation of Shandong Province (Grant No. ZR2021ZD01), and the Project of Introduction and Cultivation for Young Innovative Talents in Colleges and Universities of Shandong Province.

APPENDIX A: COMPUTATIONAL METHODS AND DETAILS

Furthermore, here, some basic quantities relating to the electron-phonon interaction are described. The imaginary part of the phonon self-energy within the Migdal approximation can be calculated with

$$\Pi''_{\mathbf{q}\nu} = \mathrm{Im}\sum_{mn,\mathbf{k}} \omega_{\mathbf{k}} \left| g^{SE}_{mn,\nu}(\mathbf{k},\mathbf{q}) \right|^2 \frac{f(\epsilon_{n\mathbf{k}}) - f(\epsilon_{m\mathbf{k}+\mathbf{q}})}{\epsilon_{m\mathbf{k}+\mathbf{q}} - \epsilon_{n\mathbf{k}} - \omega_{\mathbf{q}\nu} - i\eta}. \tag{A1}$$

The electron-phonon matrix elements $g^{SE}_{mn,\nu}(\mathbf{k},\mathbf{q})$ can be obtained by

$$g^{SE}_{mn,\nu}(\mathbf{k},\mathbf{q}) = \left(\frac{\hbar}{2m_0\omega_{\mathbf{q}\nu}}\right)^{\frac{1}{2}} g^{\nu}_{mn}(\mathbf{k},\mathbf{q}), \tag{A2}$$

in which

$$g^{\nu}_{mn}(\mathbf{k},\mathbf{q}) = \langle \psi_{m\mathbf{k}+\mathbf{q}} | \partial_{\mathbf{q}\nu} V | \psi_{n\mathbf{k}} \rangle. \tag{A3}$$

The $\psi_{n\mathbf{k}}$ is electronic wave function for band m, wave vector $\mathbf{k}$, and eigenvalue $\epsilon_{n\mathbf{k}}$. $\partial_{\mathbf{q}\nu} V$ is the derivative of the self-consistent potential associated with a phonon of wave vector $\mathbf{q}$, branch index ν, and frequency $\omega_{\mathbf{q}\nu}$. The factors $f(\epsilon_{n\mathbf{k}}, f(\epsilon_{m\mathbf{k}+\mathbf{q}}))$ are the Fermi occupations and $\omega_{\mathbf{k}}$ are the weights of the $\mathbf{k}$ points normalized to 2 in order to account for the spin degeneracy in spin-unpolarized calculations. One widely used approximation for the phonon self-energy involves neglecting the phonon frequencies $\omega_{\mathbf{q}\nu}$ in the denominator and taking the limit of a small broadening parameter η. The total EPC λ is calculated as the BZ average of the mode-resolved coupling strengths $\lambda_{\mathbf{q}\nu}$:

$$\lambda = \sum_{\mathbf{q}\nu} \omega_{\mathbf{q}} \lambda_{\mathbf{q}\nu}, \tag{A4}$$

where the $\omega_{\mathbf{q}}$ are the BZ weights associated with the phonon wave vectors $\mathbf{q}$. The $\lambda_{\mathbf{q}\nu}$ representing the EPC strength associated with a specific phonon mode and wave vector is given by

$$\lambda_{\mathbf{q}\nu} = \frac{1}{N_F \omega_{\mathbf{q}\nu}} \sum_{mn,\mathbf{k}} \omega_{\mathbf{k}} \left| g^{SE}_{mn,\nu}(\mathbf{k},\mathbf{q}) \right|^2 \delta(\epsilon_{n\mathbf{k}}) \delta(\epsilon_{m\mathbf{k}+\mathbf{q}}), \tag{A5}$$

where δ is the Dirac delta function. And it can be associated with the $\Pi''_{\mathbf{q}\nu}$ as follows:

$$\lambda_{\mathbf{q}\nu} = \frac{1}{\pi N_F} \frac{\Pi''_{\mathbf{q}\nu}}{\omega^2_{\mathbf{q}\nu}}. \tag{A6}$$

The Eliashberg spectral function α^2F can be calculated in terms of the mode-resolved coupling strengths $\lambda_{\mathbf{q}\nu}$ and phonon frequencies using

$$\alpha^2F(\omega) = \frac{1}{2} \sum_{\mathbf{q}\nu} \omega_{\mathbf{q}} \omega_{\mathbf{q}\nu} \lambda_{\mathbf{q}\nu} \delta(\omega - \omega_{\mathbf{q}\nu}). \tag{A7}$$

The anisotropic Migdal-Eliashberg theory [62,69,70] for electron-phonon superconductors can be solved with

$$Z(\mathbf{k}, i\omega_n) = 1 + \frac{\pi T}{N_F \omega_n} \sum_{\mathbf{k}'n'} \frac{\omega'_n}{\sqrt{\omega'^2_n + \Delta^2(\mathbf{k}', i\omega'_n)}} \times \lambda(\mathbf{k}, \mathbf{k}', n - n') \delta(\epsilon_{\mathbf{k}'}), \tag{A8}$$

$$Z(\mathbf{k}, i\omega_n) \quad \Delta(\mathbf{k}, i\omega_n) = \frac{\pi T}{N_F} \sum_{\mathbf{k}'n'} \frac{\Delta(\mathbf{k}', i\omega'_n)}{\sqrt{\omega'^2_n + \Delta^2(\mathbf{k}', i\omega'_n)}} \times [\lambda(\mathbf{k}, \mathbf{k}', n - n') - N_F V(\mathbf{k} - \mathbf{k}')] \delta(\epsilon_{\mathbf{k}'}). \tag{A9}$$

In the equations, T, Z, and Δ represent the absolute temperature, the renormalization function, and the superconducting gap, respectively. N_F is the DOS of electrons at the E_F and $\delta(\epsilon_{\mathbf{k}})$ is the Dirac delta function. $\mathbf{k}$ denotes the composite band wave vector and $i\omega_n = i(2n + 1)\pi T$ are the fermion Matsubara frequencies. The anisotropic EPC matrix $\lambda(\mathbf{k}, \mathbf{k}', n - n')$ can be obtained by

$$\lambda(\mathbf{k}, \mathbf{k}', n - n') = \int_0^{\max} \frac{2\omega}{(\omega - \omega'_n)^2 + \omega^2} \alpha^2F(\mathbf{k}, \mathbf{k}', \omega) d\omega, \tag{A10}$$

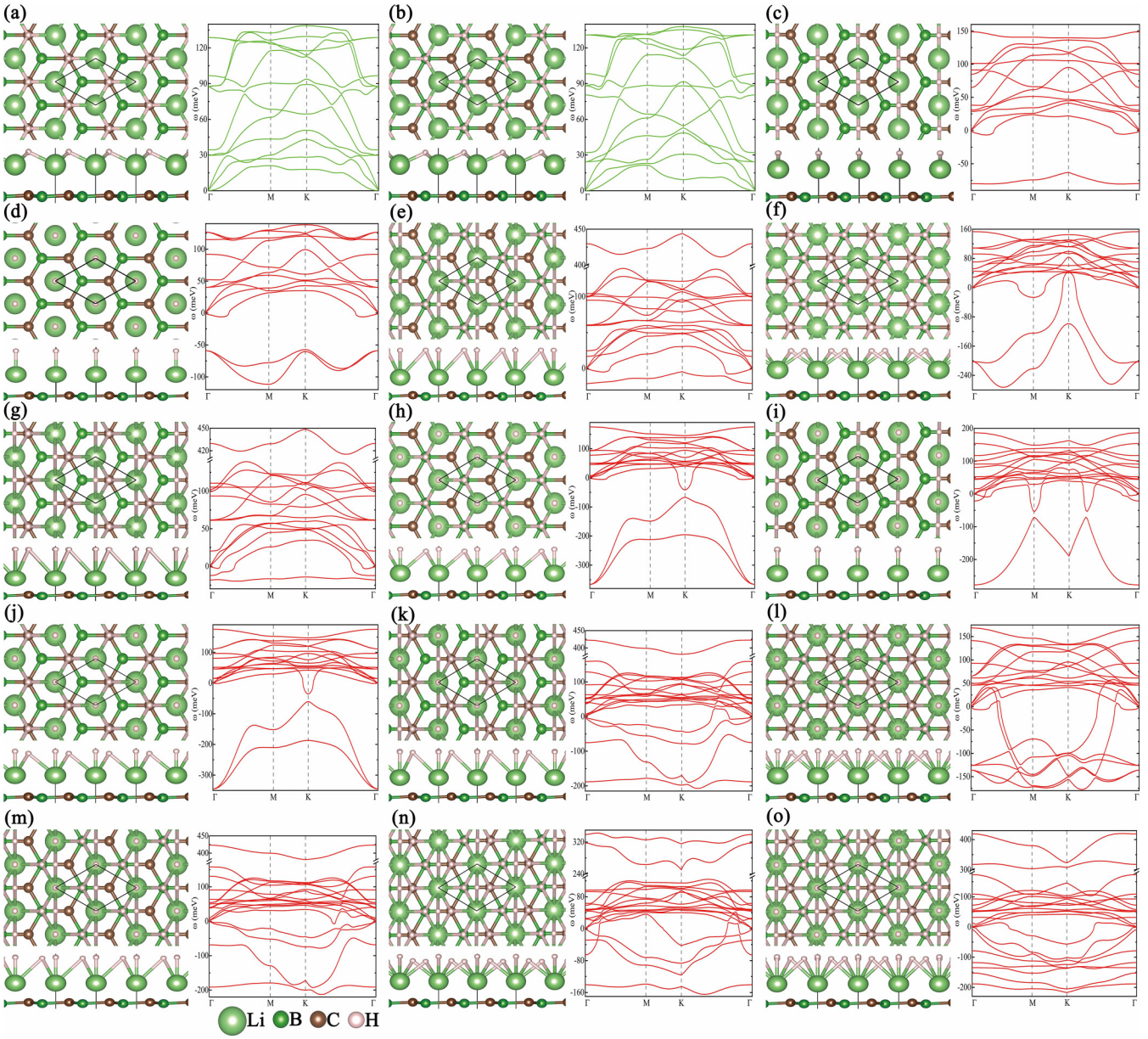

FIG. 6. Different configuratons of hydrogenated monolayer LiBC for (a)–(d) one, (e)–(j) two, (k)–(n) three, and (o) four H adatoms in a unit cell. In each picture, a top and side views of structures are shown in the left and the corresponding phonon dispersions are depicted in the right.

where $\alpha^2F(\mathbf{k}, \mathbf{k}', \omega)$ can be given:

$$\alpha^2F(\mathbf{k}, \mathbf{k}', \omega) = N_F \sum_{\nu} \left|g^{SE}_{mn,\nu}(\mathbf{k}, \mathbf{q})\right|^2 \delta(\omega - \omega_{\mathbf{k}-\mathbf{k}',\nu}). \tag{A11}$$

The Morel-Anderson pseudopotential μ^* is a semiempirical parameter to solve the numerical solution of the Eliashberg equation, defined as $\mu^* = \mu^*/[1 + \mu^* \ln(\omega_{el}/\omega_{ph})]$, where ω_{el} and ω_{ph} are the characteristic electron and phonon energy, respectively, and μ^* is the Coulomb potential. A reasonable value is in the range of 0.1–0.2 [62]. In this work, we set a typical value of $\mu^* = 0.1$ [65,69,80,81]. The Dirac δ functions for electrons and phonons were smeared out by a Gaussian function with widths of 50 and 0.05 meV, respectively.

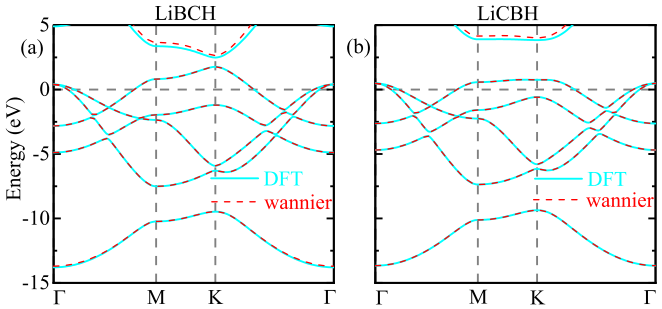

FIG. 7. Band structures for (a) LiBCH and (b) LiCBH obtained from DFT calculation (cyan solid lines) and Wannier function (red dotteda lines), respectively.

TABLE III. Calculated cohesive (E_{coh}), formation (E_{for}) energies (eV/atom), and the change in total energy (ΔE/eV).

	Parameters	E_{coh}	E_{for1}	E_{for2}	ΔE_1	ΔE_2	ΔE_3
Materials	LiBCH	−5.103	−0.348	−0.633	−1.457	1.154	2.698
	LiCBH	−5.083	−0.328	−0.613	−1.298	1.075	2.619

APPENDIX B: POSSIBLE CRYSTAL STRUCTURE ANALYSIS

The hydrogenation of a monolayer of LiBC on the Li side has been investigated systematically, yielding several possible structures. Within the LiBC unit cell, there are four high-symmetry atomic positions occupied by H adatoms, namely positions above the atoms of B, C, Li, and the bridge of B and C atoms. All possible configurations with one to four H adatoms per unit cell of LiBC, namely $LiBCH_x$ ($x = 1$, 2, 3, 4), have been considered. Their structures within top and side views are described in Fig. 6. For these structures, there are only two combinations which possess dynamical stabilities, indicating hydrogenated LiBC where H occupies a single honeycomb sublattice site above (a) C atom and (b) B atom. Thus the two structures are studied in the paper.

APPENDIX C: TIGHT-BINDING MODELS OF PRISTINE LiBCH AND LiCBH

See Fig. 7 and Table I for tight-binding models of pristine LiBCH and LiCBH.

APPENDIX D: PARAMETERS OF CRYSTAL STRUCTURE

In detail, the crystal structures of the monolayers LiBCH and LiCBH consist of three atom layers stacking in the order C(B)-Li-H. The perpendicular distances between the C and Li atoms of LiBCH and LiCBH h are 1.7893 and 1.9048 Å, respectively. Moreover, a minor wrinkle between C and B atoms indeed emerges here, namely Δh_1. The Δh_1 of LiBCH and LiCBH are 0.0659 and 0.0058 Å, respectively. Thus it seems that the C and B graphenelike net of LiCBH is flatter than that of LiBCH. The reason for this will be explored in the following part of the charge transfer. Moreover, the perpendicular distances between the Li and H atoms Δh_2 of them are 0.7490 and 0.7249 Å, respectively. Both are crystallized in the same space group of $P3m1$ (No. 156). The unit cell comprising four atoms is enclosed in a black rhombus with a solid line. In a unit cell, a C (B) atom is bonded with three B (C) atoms. The Li atom is located at the hollow site of the graphenelike net and bonded with three H atoms. The lattice constants of LiBCH and LiCBH are 2.7258 and 2.7255 Å, respectively.

APPENDIX E: STRUCTURAL STABILITY

1. Cohesive and formation energies: Thermodynamic stability

First, it is widely useful for cohesive energy to evaluate the covalent bond strength and the stability of LiBCH and LiCBH. The cohesive energy can be expressed by the following formula:

$$E_{coh} = \frac{E_{tot} - (E_{Li} + E_B + E_C + E_H)}{4}, \tag{E1}$$

where E_{tot} is the total energy of LiBCH and LiCBH; E_{Li}, E_B, E_C, and E_H are the isolated atomic energies of Li, B, C, and H atoms, respectively; "4" is the total atomic number of a unit cell. The calculated cohesive energies for LiBCH and LiCBH are −5.103 and −5.083 eV/atom, respectively. It is found that both structures of LiBCH are energetically favorable and LiBCH is the more energetically stable monolayer. For comparison, the calculated cohesive energies of the previously theoretically predicted 2D materials for Ga_2SO_2, Ga_2SSe_2, and Ga_2STe_2, at the same theoretical level, are −5.24, −4.13, and −3.77 eV/atom [82], respectively. More meaningfully, similar or larger cohesive energies of the later experimentally fabricated well-known 2D materials, such as MoS_2 (−5.14 eV/atom) [83], siliene (−3.90 eV/atom) [84], antimonene (−2.64 eV/atom) [85], black phosphorene (−3.48 eV/atom) [86,87], Cu_2Si (−3.46 eV/atom) [88], arsenene (−2.97 eV/atom) [89], In_2Se_3 (−3.36 eV/atom) [90–92], bismuthene (−2.46 eV/atom) [93], and so on, indicate that it is possible to synthesize our predicted LiBCH and LiCBH under appropriate experimental conditions.

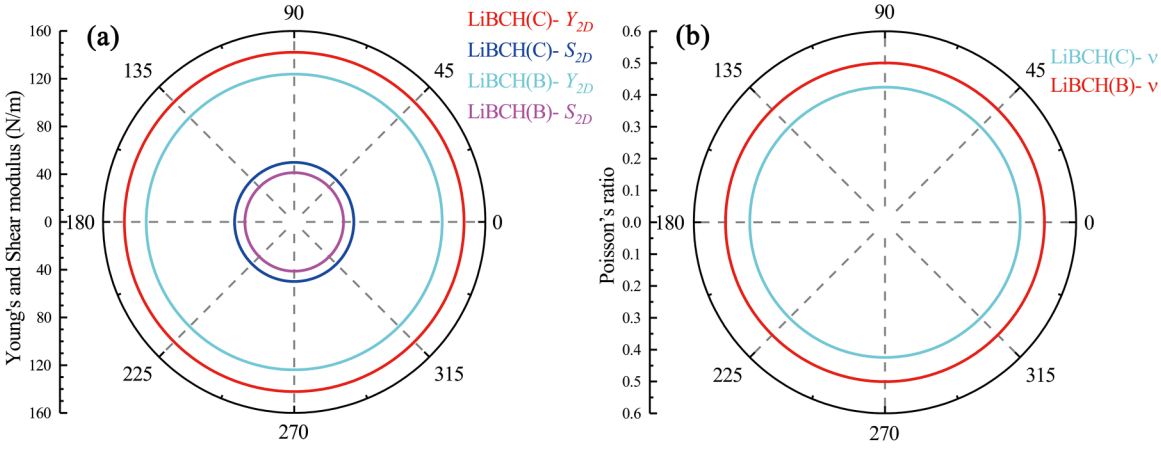

FIG. 8. Polar diagrams for (a) Young's modulus Y_{2D}, (a) Shear modulus S_{2D}, and (b) Poisson's ratio υ of LiBCH and LiCBH.

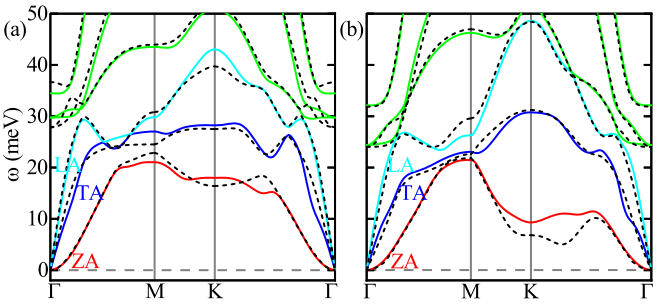

FIG. 9. Phonon spectra from 0 to 50 meV for (a) LiBCH and (b) LiCBH monolayers with the colored solid lines in the calculation of QE. For comparison, the phonon spectra with black dotted lines in the calculation of VASP are also included in the picture.

Second, to simulate possible routes for experimental synthesis, we also calculate the formation energies of LiBCH and LiCBH using the following two approaches.

One is to exfoliate monolayer LiBC from bulk LiBC and then introduce hydrogen gas (top-down approach)

$$E_{\text{for1}} = \frac{E_{\text{tot}} - \left(\frac{E_{\text{LiBC}}}{2} + \frac{E_{H_2}}{2}\right)}{4}, \tag{E2}$$

here, in which E_{LiBC} is the total energy of the experimentally synthesized bulk LiBC [18] [shown in Fig. 1(a)]; E_{H_2} is the total energy of experimentally observed gas H_2 [94] structured by magnesium and crystallized in the hexagonal $P6_3/mmc$ space group. In this case, the formation energies of LiBCH and LiCBH are −0.348 and −0.328 eV/atom, respectively.

TABLE IV. Calculated elastic constants C_{ij} (N/m), Young's modulus Y_{2D} (N/m), shear modulus S_{2D} (N/m), and Poisson's ratio υ of LiBCH and LiCBH.

	Parameters	C_{11}	C_{12}	C_{66}	Y_{2D}	S_{2D}	υ
Materials	LiBCH	173.3	73.5	49.9	142.1	49.9	0.424
	LiCBH	165.2	82.7	41.3	123.8	41.3	0.500

The other is to synthesize it using various elemental substances (down-top approach)

$$E_{\text{for2}} = \frac{E_{\text{tot}} - \left(\frac{E_{Li^{3D}}}{9} + \frac{E_{B^{3D}}}{36} + \frac{E_{C^{3D}}}{12} + \frac{E_{H_2}}{2}\right)}{4}, \tag{E3}$$

here, where $E_{Li^{3D}}$, $E_{B^{3D}}$, $E_{C^{3D}}$ are the total energy of the experimentally observed α-samarium structured bulk metal Li [95,96], α-boron structured bulk metal B [96–98], and rhombohedral graphitelike structured bulk graphite [96,99], respectively, all which crystallize in the trigonal R-3m space group. In this case, the formation energies of LiBCH and LiCBH are −0.633 and −0.613 eV/atom, respectively.

The above negativity of the formation energy value indicates the energetic favorability of the investigated monolayers, suggesting that the experimental synthesis is not only exothermic but also feasible.

Moreover, we also explore whether LiBCH and LiCBH show an energetic preference for decomposing into other structures with decreased H content, along with atomic hydrogen or hydrogen molecules. When investigating reactions in the form of A → B + C, we evaluate the change in total energy (ΔE) using the formula $\Delta E = E_B + E_C - E_A$, with E_X (X = A, B, C) denoting the total energy of compound X

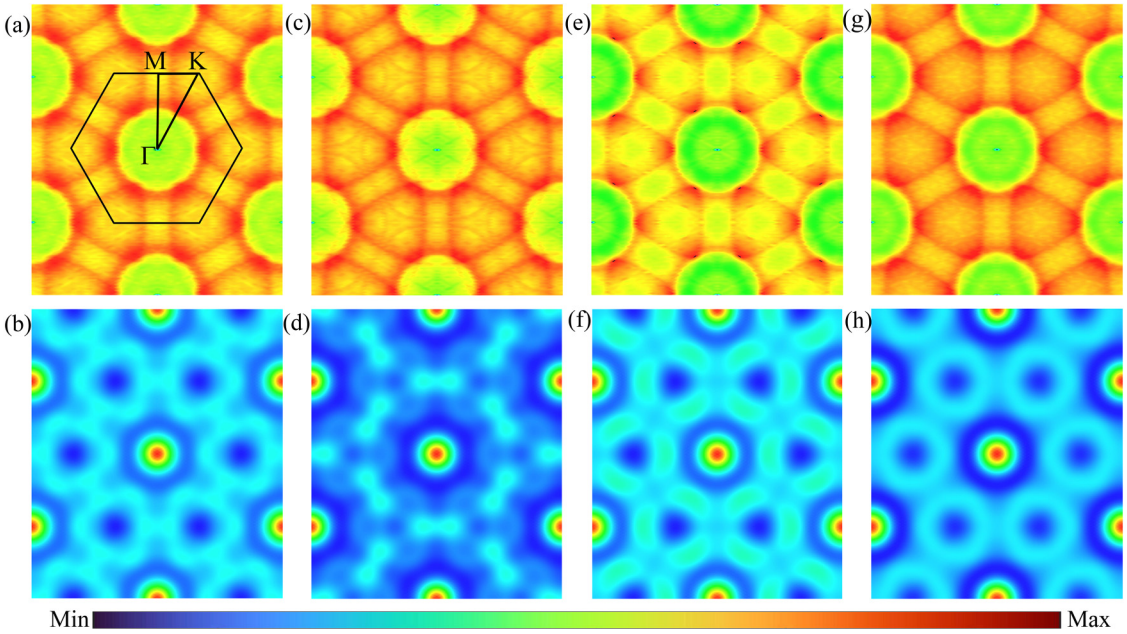

FIG. 10. (a), (c) Real part (static or bare) $\chi'(\mathbf{q})$ and (b), (d) imaginary part (Fermi nesting function) $\chi''(\mathbf{q})$ the electronic susceptibility for LiBCH, LiCBH, respectively. The corresponding electronic susceptibility for (e), (f) 2.1% LiBCH and (g), (p) 3.5% LiCBH. The value increases from blue and green to red. The first BZ and high symmetric route along with Γ-M-K-Γ is shown in black solid lines.

TABLE V. Charge associated with it according to Bader partitioning (in units of $|e|$) for each atom in LiBCH and LiCBH. ZVAL represents valence electrons of isolated atoms in the pseudopotentials. Differences between charge and ZVAL for LiBCH and LiCBH are denoted by Δe(C) and Δe(B), respectively, the symbol "+" ("−") of which shows charge gain (loss).

Atoms	ZVAL	LiBCH	Δe(C)	LiCBH	Δe(B)
B	3	1.216	−1.784	1.235	−1.765
C	4	6.066	+2.066	6.017	+2.017
Li	1	0.192	−0.808	0.191	−0.809
H	1	1.526	+0.52	1.557	+0.557

obtained via DFT:

$$2\mathrm{LiBCH_2} \rightarrow \mathrm{H_2} + 2\mathrm{LiBCH}. \tag{E4}$$

The references can be obtained as follows: $LiBCH_2$ from Fig. 6(f), gas H_2 from [96], and LiBCH from Figs. 6(a) and 6(b). The calculated change in total energy of LiBCH and LiCBH are −1.457 (ΔE_{1C}) and −1.298 (ΔE_{1B}) eV, respectively. Hence $LiBCH_2$ tends to energetically prefer the expulsion of H adatoms in the form of hydrogen gas, thereby generating LiBCH and LiCBH. Additionally, this finding confirms the dynamical instability [Fig. 6(f)] of the structure $LiBCH_2$ to the left side of reaction

$$2\mathrm{LiBCH} \rightarrow \mathrm{H_2} + 2\mathrm{LiBC}. \tag{E5}$$

The monolayer LiBC, shown in Fig. 1(b), can be fully optimized from DFT. The calculated change in total energy of LiBCH and LiCBH are 1.154 (ΔE_{2C}) and 1.075 (ΔE_{2B}) eV, respectively. Therefore, the fact that this reaction does not result in further reduction of internal energy provides evidence for the thermodynamic stability of LiBCH and LiCBH:

$$\mathrm{LiBCH} \rightarrow \mathrm{H} + \mathrm{LiBC}. \tag{E6}$$

The H is the isolated atom obtained from formula (13). The calculated change in total energy of LiBCH and LiCBH are 2.698 (ΔE_{3C}) and 2.619 (ΔE_{3B}) eV, respectively. Therefore, over the perspective of energy, the cost of dehydrogenation of LiBCH and LiCBH as the form of H atom is adverse.

Hence the energy consideration indicates that the formation of hydrogen gas [H_2, formula (17)] and atomic hydrogen [H, formula (18)] from the ground state structure of LiBCH and LiCBH is not thermodynamically favorable. It is obvious that the LiBCH and LiCBH that we investigated are energetic preferred structures. The above related parameters can be obtained in Table III.

In brief, for three perspectives of cohesive energy, formation energy, and energetic preference, we fully prove that the LiBCH and LiCBH possess the thermodynamic stability and possibility of experimental synthesis.

2. Elastic constants: Mechanical stability

Furthermore, based on the calculation of elastic constants C_{ij}, we also determine the mechanical stability of LiBCH and LiCBH. Due to the symmetric structure (space group $P3m1$) of them, half of the four independent elastic constants (C_{11}, C_{12}, C_{22}, and C_{66}), namely C_{11} and C_{12}, have to be calculated. This is attributed to $C_{22} = C_{11}$, $C_{12} = C_{21}$, and C_{66} can be obtained from the formula of $C_{66} = (C_{11} - C_{12})/2$. Next, with the calculated elastic constants and Born criteria, we can evaluate the mechanical stability of the investigated materials. Other elastic parameters, involving Yong's Y_{2D} and shear modulus S_{2D}, and Poisson's ratio υ, can be calculated with the former elastic constants C_{ij}, following the formulas [100]

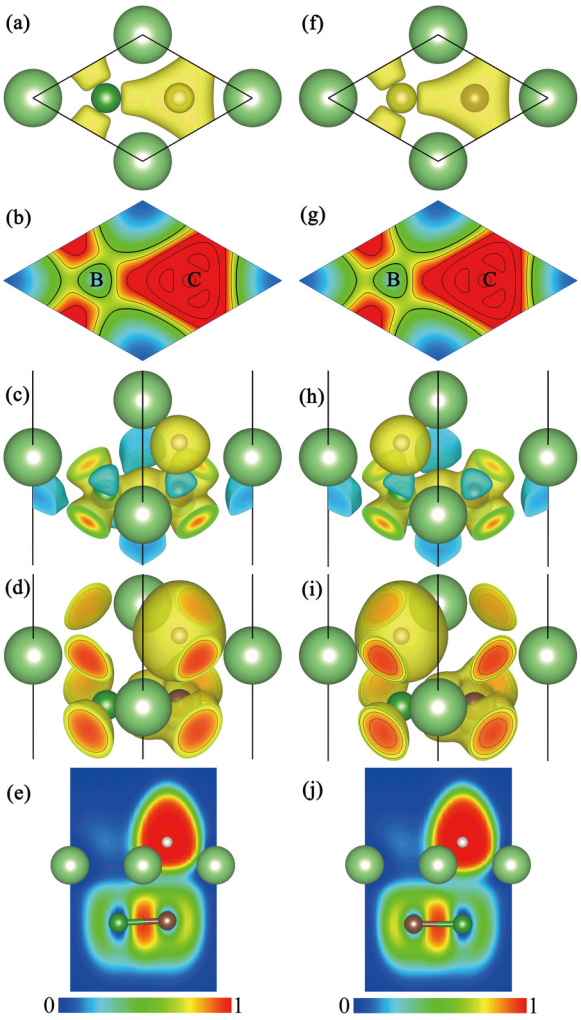

FIG. 11. (a), (f) Space electron density; (b), (g) 2D charge density display in B and C atomic plane; (c), (h) charge density difference relative to the superposition of space electron density; (d), (i) electron localization function (ELF) of the total electron density (isovalue 0.65); (e), (j) 2D ELF maps of the (110) plane generated by Li, C, B, and H atoms, for LiBCH and LiCBH, respectively. The dark green, brown, light green, and pink spheres represent B, C, Li, and H atoms, respectively.

$$Y_{2D} = \frac{C_{11}^2 - C_{12}^2}{C_{11}}, \tag{E7}$$

$$S_{2D} = C_{66} = \frac{C_{11} - C_{12}}{2}, \tag{E8}$$

$$\upsilon = \frac{C_{12}}{C_{11}}. \tag{E9}$$

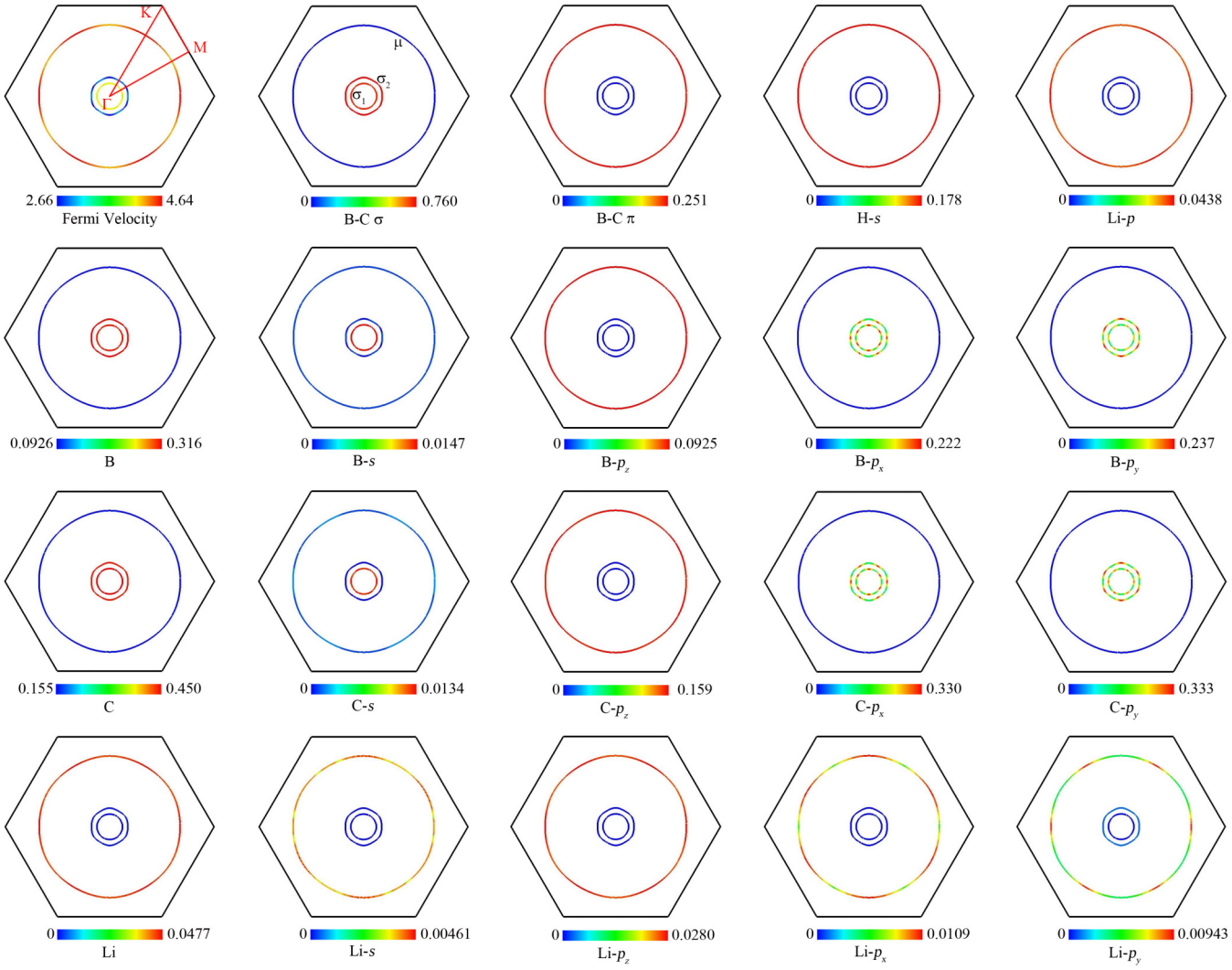

FIG. 12. FSs of LiBCH with different indexes, which are listed at the bottom of subgraphs. The numerical values represent the weight of different indexes and increases from blue to red. The high symmetric route along with Γ-*M*-*K*-Γ is shown in the first subgraph with the index of Fermi velocity.

Theoretically, applying small strains to the fully optimized structures, the elastic constants can be extracted from the energy variation, where the method accords well with other 2D materials [82,101,102]. In this paper, the strain from −0.015 to +0.015 with a step of 0.005 is used to valuate the strain dependence of elastic energy.

Table IV shows the calculated elastic parameters of LiBCH and LiCBH. It is demonstrated that the structures of LiBCH and LiCBH with elastic constants obey Born's criteria [100] for mechanical stability, that is, $C_{11} > 0$ and $C_{11}^2 - C_{12}^2 > 0$. It is obvious that the investigated structures are mechanically stable. In addition, the Young's modulus of LiBCH and LiCBH are 142.1 and 123.8 N/m, respectively, which are comparable with the ones of GeC (140.1 N/m) [100], BeC (145.5 N/m) [103], and MoS_2 (130 N/m) [104] monolayers and less than that of SiC (163.5 N/m) [100] monolayer and graphene (340 N/m) [105]. In other words, compared to graphene or SiC monolayer, the structures exhibit greater flexibility and can tolerate deformations with larger amplitudes.

Polar diagrams for Y_{2D}, S_{2D}, and υ of LiBCH and LiCBH are drawn in Fig. 8. The flawless circular shapes observed in the angle-dependent Young's, Shear modulus, and Poisson's ratio plots indicate that the materials mechanical properties are not influenced by the angle, as the consequence of in-plane isotropy of LiBCH and LiCBH. It is also similar to other isotropic structures, for instance, graphene [106] and hexagonal Janus [107–109].

APPENDIX F: PHONON SPECTRA—DYNAMIC STABILITY

Last, the simulated phonon spectra play a significant role in determining the dynamic stability of a new 2D material. As shown in Fig. 9, based on the DFTP method in QE (colored solid lines) and the Vienna *ab initio* simulation package (VASP) [110] (black dotted lines) code, we also investigate the phonon spectra from 0 to 50 meV of LiBCH and LiCBH along the high-symmetry points Γ-*M*-*K*-Γ in the BZ. An imaginary frequency is assigned to indicate the presence of an unstable

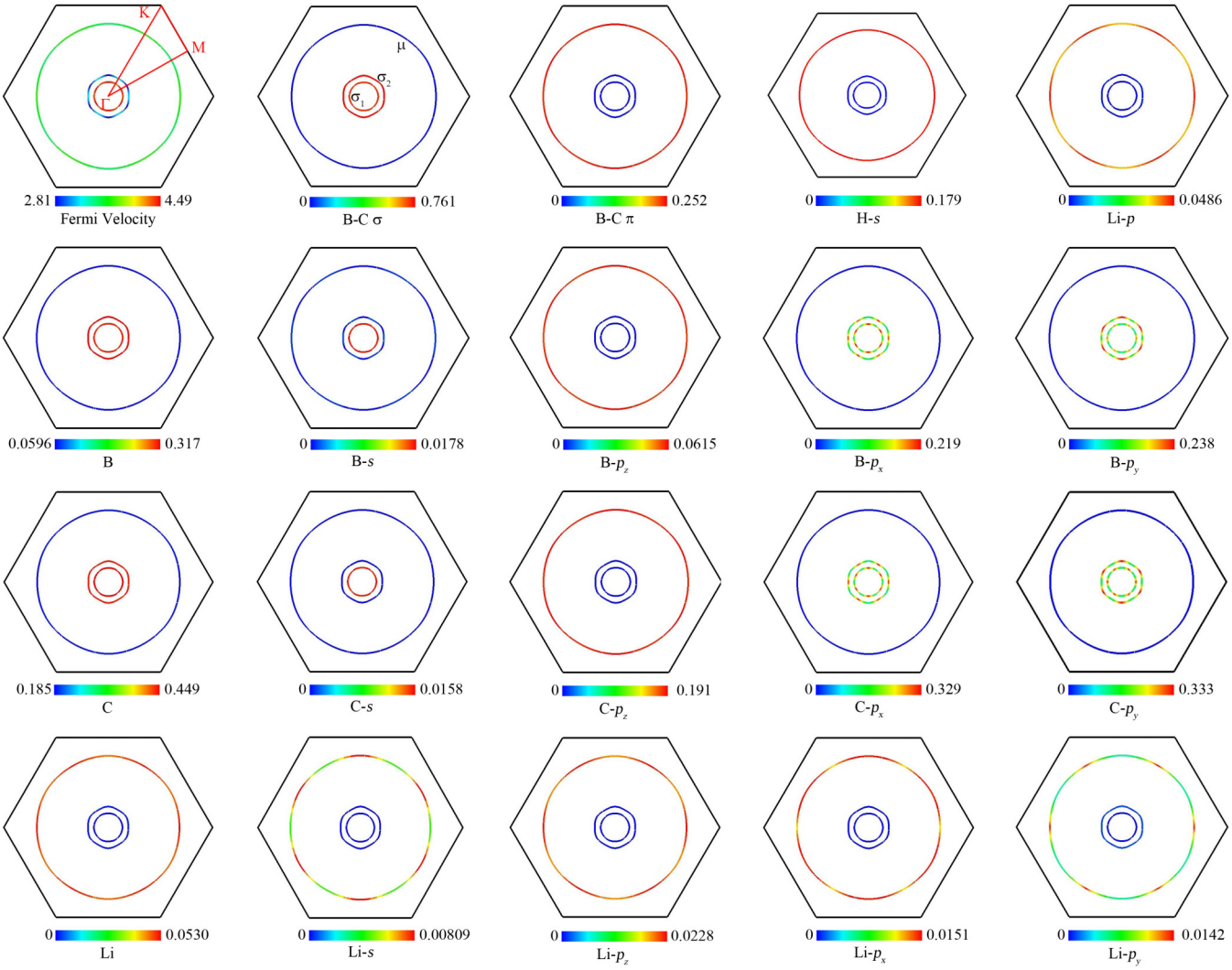

FIG. 13. FSs of LiCBH with different indexes, which are listed at the bottom of subgraphs. The numerical values represent the weight of different indexes and increases from blue to red. The high symmetric route along with Γ-*M*-*K*-Γ is shown in the first subgraph with the index of Fermi velocity.

phonon mode. In fact, no imaginary frequency appears in the partial phonon spectra of Fig. 9, whether QE or VASP in the calculations. Thus the provided evidence thoroughly demonstrates the dynamic stabilities of LiBCH and LiCBH.

APPENDIX G: ELECTRONIC SUSCEPTIBILITY

Generally, the real and imaginary parts of electronic susceptibility, which draw from the full energy range and the low-frequency region, respectively, are used to characterize the stability of the electronic system [111,112] and FS nesting [42]. They can be calculated [42] by the following two formulas:

$$\chi'(\mathbf{q}) = \sum_k \frac{f(\epsilon_{\mathbf{k}}) - f(\epsilon_{\mathbf{k+q}})}{\epsilon_{\mathbf{k}} - \epsilon_{\mathbf{k+q}}}, \tag{G1}$$

$$\lim_{\omega\to 0} \chi''(\mathbf{q},\omega)/\omega = \sum_{\mathbf{k}} \delta(\epsilon_{\mathbf{k}} - \epsilon_{\mathbf{F}})\delta(\epsilon_{\mathbf{k+q}} - \epsilon_{\mathbf{F}}), \tag{G2}$$

respectively. Here, $\epsilon_{\mathbf{k}}$ ($\epsilon_{\mathbf{k+q}}$) and $\epsilon_{\mathbf{F}}$ are band energies measured from the E_F at the wave vectors $\mathbf{k}$ ($\mathbf{k+q}$) and the Fermi energy, respectively.

As shown in Figs. 10(a) and 10(c) of $\chi'(\mathbf{q})$, the regions with strong values appear around the BZ boundary. It means that the stability of the electronic system comes from the B-C graphenelike net. As for $\chi''(\mathbf{q})$ of Figs. 10(b) and 10(d), it maps all complete FS nests to themselves at the Γ point, which has no tangible physical significance [42]. Other slightly strong values occur both around and in between the B/C atoms. While due to the absence of obvious peaks of nesting function and in conjunction with Figs. 2(b) and 2(c), it does not provide significant benefits for EPC, unlike Janus MoSH [42] and 1*T*-VSe_2 [113].

APPENDIX H: ELECTRONIC PROPERTY

The above subsection fully proves the stability of investigated monolayers. Here, the overall analysis of electronic property can be implemented step by step in this subsection.

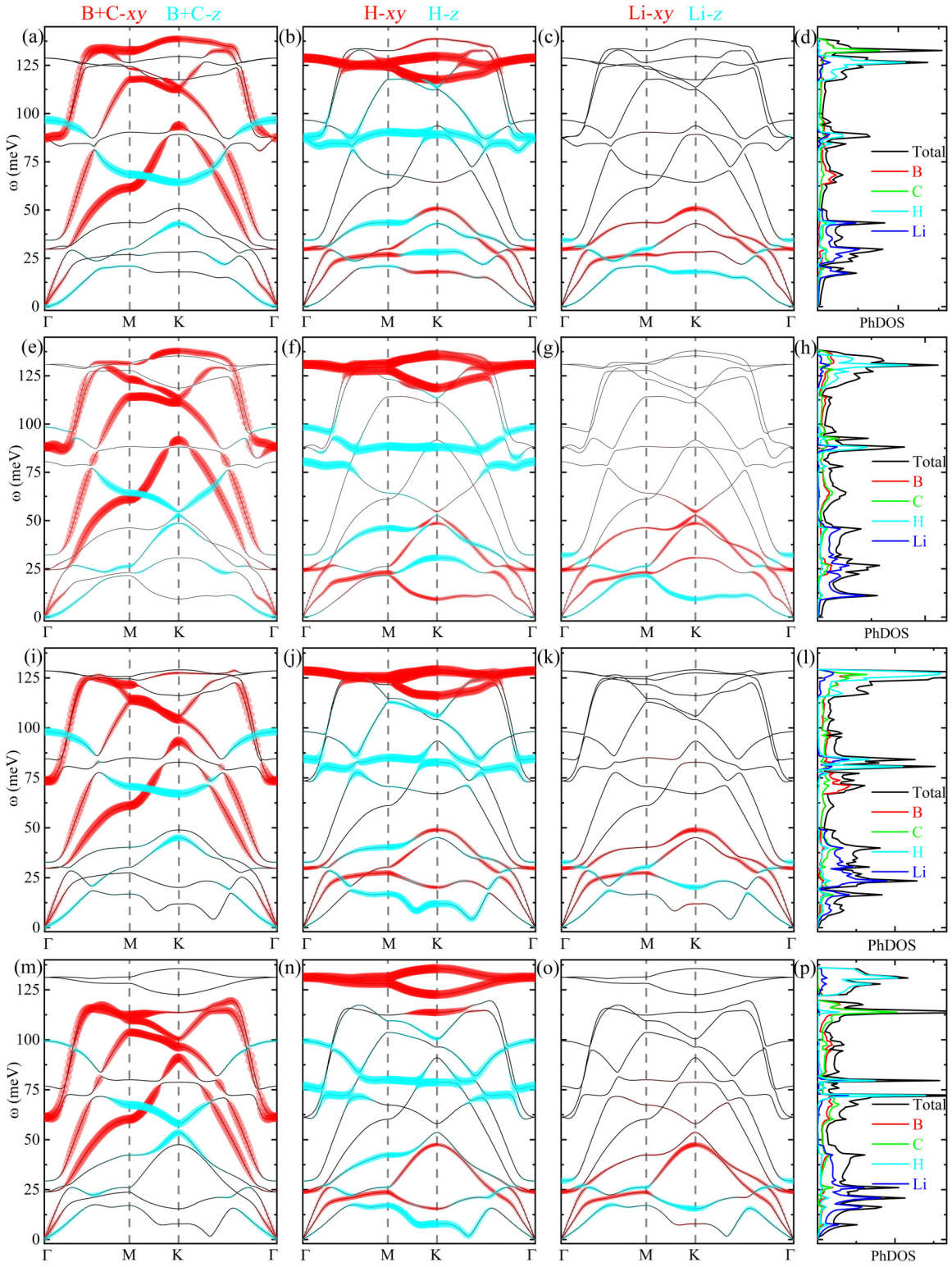

FIG. 14. Calculated phonon dispersions weighted with atomic vibrations for (a)–(c) LiBCH and (e)–(g) LiCBH. *xy* and *z*, shown as red and cyan, are in-plane and out-of-plane atomic vibrations, respectively. Projected PhDOSs for (d) LiBCH and (h) LiCBH. The black, red, green, cyan, and blue colors represent the vibration distributions of total, B, C, H, and Li atoms, respectively. The corresponding atomic vibrations' directions for (i)–(l) 2.1% LiBCH and (m)–(p) 3.5% LiCBH.

1. Distribution and transfer of charge

First, based on the Bader charge [114] calculation, the quantitative charge transformations for each atom of LiBCH and LiCBH are shown in Table V. Charge acquisition occurs in C and H atoms, while B and Li atoms undergo charge loss. In detail, the charge gains for C and H atoms of LiBCH

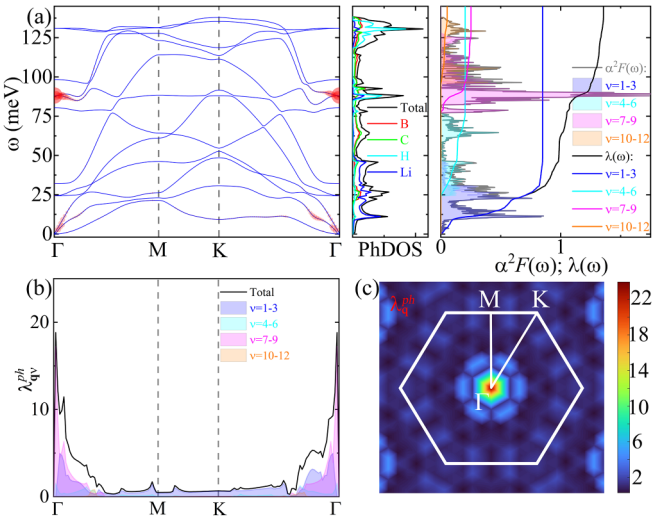

FIG. 15. Properties of lattice dynamics and EPC for the monolayer LiCBH. (a) Phonon weighted with the EPC parameters $\lambda_{\mathbf{q}}^{ph}$ (red), PhDOS, and the total EPC $\lambda(\omega)$ with the corresponding mode-resolved Eliashberg spectral function $\alpha^2F(\omega)$. (b) EPC $\lambda_{\mathbf{q}\nu}^{ph}$ along the high-symmetry points Γ-*M*-*K*-Γ. (c) EPC $\lambda_{\mathbf{q}}^{ph}$ projected in the whole BZ.

(LiCBH) are 2.066 (2.017) and 0.526 (0.557) electron, respectively; the charge losses for B and Li atoms of LiBCH (LiCBH) are 1.784 (1.765) and 0.808 (0.809) electron, respectively. With different sites of H atoms, there is a minor distinction: C atoms of LiBCH can accumulate slightly more charges than those of LiCBH. Generally, the charges are transferred from B and Li atoms to C and H atoms.

Next, charge information can be obtained in Fig. 11. As shown in Figs. 11(a) and 11(f), space charge density distributions of LiBCH and LiCBH, charges congregate around C, H atoms and B-C bonds. This is in harmony with the conclusion drawn from Bader charge calculation. In order to gain a clearer understanding of the charge density distribution in the B and C atomic planes, as depicted in Figs. 11(b) and 11(g), we also provide their 2D charge density displays, in which the charge density increases from blue to red and the black lines are the contour lines. It is also observed that there is less charge exiting around the B atoms, while the region in between the B and C atoms, as well as around the C atoms, exhibits denser contour lines, indicating higher charge density and possible strong covalent bonds.

To further uncover charge transformation of the different atomic orbitals, we also show charge density difference in Figs. 11(c) and 11(h). Here, yellow and blue surfaces show charge accumulation and depletion, respectively. The yellow surface emerges in the plane of B and C atoms and around the H atoms, while the blue surface resides in the hollow sites perpendicular to the B, C plane and above/below the B, C atoms. To be more precise, the B and C atomic p_z orbitals, along with the *s* orbital of the Li atom, experience the charges loss, while the p_x, p_y orbitals of C atom and *s* orbital of H atom obtain charges. Electron localization function (ELF) can provide further corroborative evidences to support this, shown in Figs. 11(d) and 11(i). Obviously, compared with the loss of the p_z orbital of C atom, more charges are injected into

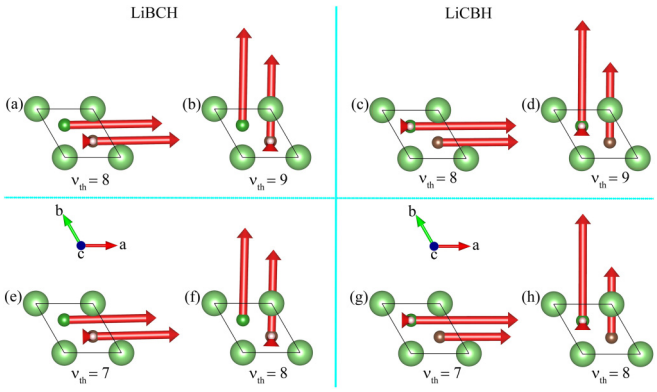

FIG. 16. Degenerate *E* modes with a frequency of 87.43 and 88.21 meV for (a), (b) LiBCH and (c), (d) LiCBH, respectively. The corresponding atomic vibrations for (e), (f) 2.1% LiBCH in 73.52 meV and (g), (h) 3.5% LiCBH in 61.28 meV.

the p_x and p_y orbitals to form the strong covalent σ bonds with B atom, seen as red regions between B and C atoms in Figs. 11(e) and 11(j). In general, this results to C and B atomic charge gain and loss, respectively, which accords well with the conclusions obtained from Bader charge and charge density distribution.

In addition, for LiBCH, there are four van Hove singularities (or saddle points) located at *M* (−2.37, −1.95, 0.82, and 3.34 eV) points, while the two near flat bands along with *M* and *K* points (around 0.61 and 3.91 eV) appear in LiCBH. They are pointed out with arrows and distinguished different dominant contribution orbitals by colors.

2. Fermi sheets and their anisotropic distribution

See Figs. 12 and 13 for Fermi sheets and their anisotropic distribution.

APPENDIX I: PHONON VIBRATION

Phonon vibration is presented in Fig. 14.

APPENDIX J: EPC PARAMETERS $\lambda_{\mathbf{q}}^{ph}$ OF LiCBH

The SDOS can be calculated with the following formula:

$$\frac{N_S(\omega)}{N_F} = \mathrm{Re}[\omega/\sqrt{\omega^2 - \Delta^2(\omega)}], \tag{J1}$$

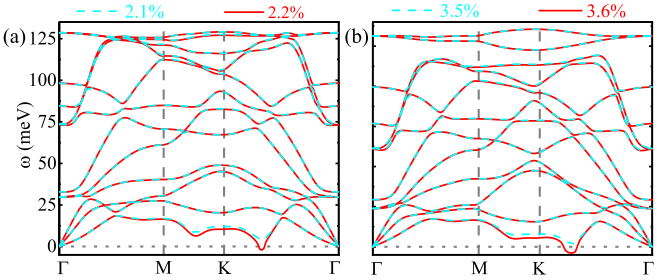

FIG. 17. Phonon spectra of (a) LiBCH and (b) LiCBH beyond the limit of biaxial stretching.

TABLE VI. Symmetry, vibration (IP and OP represent in-plane and out-of-plane, respectively), activity (I and R denote infrared and Raman activity, respectively), and frequency (ω in meV) of the nine optical vibrational modes at the Γ point.

LiBCH					LiCBH				
Modes	Symmetry	Vibration	Activity	ω	Modes	Symmetry	Vibration	Activity	ω
		0%					0%		
4,5	E	IP H and Li	$I+R$	29.76	4,5	E	IP H and Li	$I+R$	24.39
6	A_1	OP H and Li	$I+R$	34.48	6	A_1	OP Li with a little OP H	$I+R$	32.13
7	A_1	OP H	$I+R$	87.40	7	A_1	OP H	$I+R$	80.52
8,9	E	IP B/C	$I+R$	87.43	8,9	E	IP B/C	$I+R$	88.21
10	A_1	OP B/C	$I+R$	96.74	10	A_1	OP H with a little OP B/C	$I+R$	98.40
11,12	E	IP H	$I+R$	128.79	11,12	E	IP H	$I+R$	130.91
		2.1%					3.5%		
4,5	E	IP H and Li	$I+R$	29.73	4,5	E	IP H and Li	$I+R$	23.83
6	A_1	OP H and Li	$I+R$	32.83	6	A_1	OP Li with a little OP H	$I+R$	29.35
7,8	E	IP B/C	$I+R$	73.52	7,8	E	IP B/C	$I+R$	61.28
9	A_1	OP H	$I+R$	84.62	9	A_1	OP H	$I+R$	76.86
10	A_1	OP B/C	$I+R$	98.16	10	A_1	OP H with a little OP B/C	$I+R$	99.50
11,12	E	IP H	$I+R$	128.59	11,12	E	IP H	$I+R$	131.30

where "Re" represents the gap $\Delta(\omega)$ projected on the real axis. The $N_S(\omega)$ and N_F are the electron DOS of superconducting and normal states at E_F. (See also Fig. 4).

APPENDIX K: ATOM VIBRATION WITH THE DEGENERATE E MODES OF LiBCH AND LiCBH

Atom vibration with the degenerate E modes of LiBCH and LiCBH are shown in Table VI and Fig. 16.

APPENDIX L: PHONON DISPERSIONS COMPARISON FOR LiBCH AND LiCBH WITH AND WITHOUT THE BIAXIAL STRAINS

Phonon dispersions comparison for LiBCH and LiCBH with and without the biaxial strains is shown in Fig. 17.

APPENDIX M: BOOST OF T_c—THE EFFECT OF BIAXIAL STRAIN

The effect of biaxial strain is shown in Fig. 18.

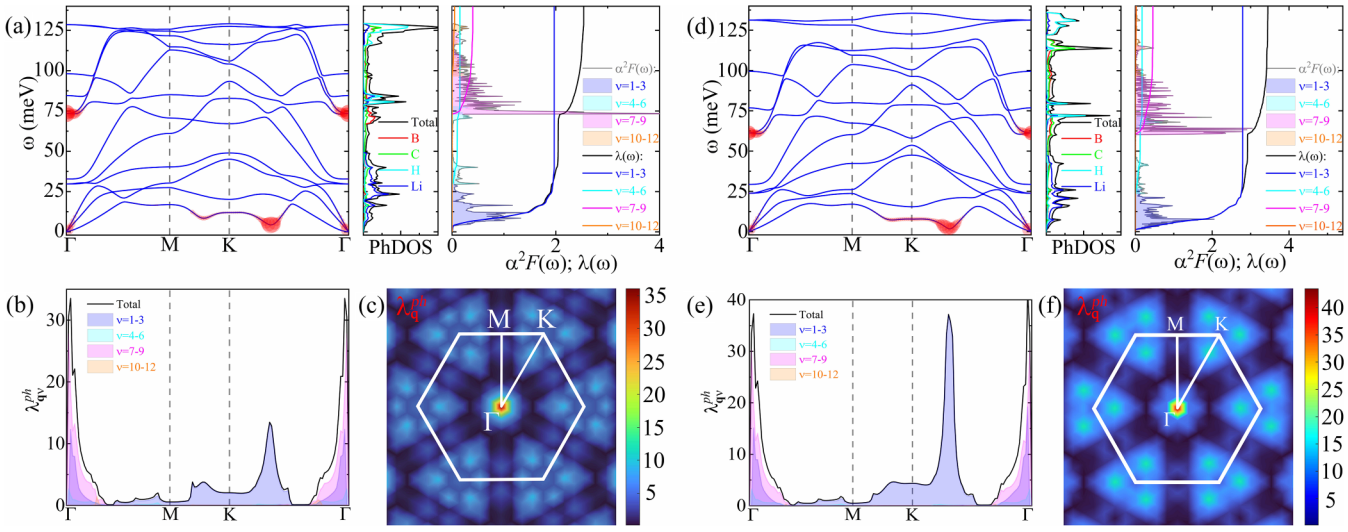

FIG. 18. Properties of lattice dynamics and EPC for LiBCH and LiCBH at the stretching limit of $\varepsilon = 2.1\%$ and 3.5% strains, respectively. For LiBCH: (a) phonon weighted with the EPC parameters $\lambda_{\mathbf{q}}^{ph}$ (red), PhDOS, and the total EPC $\lambda(\omega)$ with the corresponding mode-resolved Eliashberg spectral function $\alpha^2F(\omega)$; (b) EPC $\lambda_{\mathbf{q}\nu}^{ph}$ along the high-symmetry points Γ-M-K-Γ; (c) EPC $\lambda_{\mathbf{q}}^{ph}$ projected in the whole BZ. (d)–(f) The corresponding properties for LiCBH at $\varepsilon = 3.5\%$ strain.

[1] H. Suhl, B. T. Matthias, and L. R. Walker, Bardeen-cooper-schrieffer theory of superconductivity in the case of overlapping bands, Phys. Rev. Lett. **3**, 552 (1959).

[2] M. V. Milošević and A. Perali, Emergent phenomena in multicomponent superconductivity: An introduction to the focus issue, Supercond. Sci. Technol. **28**, 060201 (2015).

[3] L. Komendová, Y. Chen, A. A. Shanenko, M. V. Milošević, and F. M. Peeters, Two-band superconductors: Hidden criticality deep in the superconducting state, Phys. Rev. Lett. **108**, 207002 (2012).

[4] E. Babaev, Vortices with fractional flux in two-gap superconductors and in extended Faddeev model, Phys. Rev. Lett. **89**, 067001 (2002).

[5] J. Garaud, J. Carlström, and E. Babaev, Topological solitons in three-band superconductors with broken time reversal symmetry, Phys. Rev. Lett. **107**, 197001 (2011).

[6] R. M. da Silva, M. V. Milošević, A. A. Shanenko, F. M. Peeters, and J. Albino, Giant paramagnetic Meissner effect in multiband superconductors, Sci. Rep. **5**, 12695 (2015).

[7] N. V. Orlova, A. A. Shanenko, M. V. Milošević, F. M. Peeters, A. V. Vagov, and V. M. Axt, Ginzburg-Landau theory for multiband superconductors: Microscopic derivation, Phys. Rev. B **87**, 134510 (2013).

[8] J. Nagamatsu, N. Nakagawa, T. Muranaka, Y. Zenitani, and J. Akimitsu, Superconductivity at 39 K in magnesium diboride, Nature (London) **410**, 63 (2001).

[9] J. Bardeen, L. N. Cooper, and J. R. Schrieffer, Theory of superconductivity, Phys. Rev. **108**, 1175 (1957).

[10] C. Y. Pei, J. F. Zhang, C. S. Gong, Q. Wang, L. L. Gao, Y. Zhao, S. J. Tian, W. Z. Cao, C. H. Li, Z. Y. Lu, H. C. Lei, K. Liu, and Y. P. Qi, Distinct superconducting behaviors of pressurized WB_2 and ReB_2 with different local B layers, Sci. China Phys. Mech. Astron. **65**, 287412 (2022).

[11] J. Lim, A. C. Hire, Y. Quan, J. S. Kim, S. R. Xie, S. Sinha, R. S. Kumar, D. Popov, C. Park, R. J. Hemley, Y. K. Vohra, J. J. Hamlin, R. G. Hennig, P. J. Hirschfeld, and G. R. Stewart, Creating superconductivity in WB_2 through pressure-induced metastable planar defects, Nat. Commun. **13**, 7901 (2022).

[12] M. Kayhan, E. Hildebrandt, M. Frotscher, A. Senyshyn, K. Hofmann, L. Alff, and B. Albert, Neutron diffraction and observation of superconductivity for tungsten borides, WB and W_2B_4, Solid State Sci. **14**, 1656 (2012).

[13] C. Y. Pei, J. F. Zhang, Q. Wang, Y. Zhao, L. L. Gao, C. S. Gong, S. J. Tian, R. T. Luo, M. T. Li, W. G. Yang, Z. Y. Lu, H. C. Lei, K. Liu, and Y. P. Qi, Pressure-induced superconductivity at 32 K in MoB_2, Natl. Sci. Rev. **10**, nwad034 (2023).

[14] M. Gao, Z. Y. Lu, and T. Xiang, Prediction of phonon-mediated high-temperature superconductivity in $Li_3B_4C_2$, Phys. Rev. B **91**, 045132 (2015).

[15] H. Choi, D. Roundy, H. Sun, M. L. Cohen, and S. G. Louie, The origin of the anomalous superconducting properties of MgB_2, Nature (London) **418**, 758 (2002).

[16] J. M. An and W. E. Pickett, Superconductivity of MgB_2: Covalent bonds driven metallic, Phys. Rev. Lett. **86**, 4366 (2001).

[17] Y. Kong, O. V. Dolgov, O. Jepsen, and O. K. Andersen, Electron-phonon interaction in the normal and superconducting states of MgB_2, Phys. Rev. B **64**, 020501(R) (2001).

[18] M. Wörle, R. Nesper, G. Mair, M. Schwarz, and H. G. Von Schnering, LiBC-ein vollstandig interkalierter Heterographit, Z. anorg. allg. Chem. **621**, 1153 (1995).

[19] P. Ravindran, P. Vajeeston, R. Vidya, A. Kjekshus, and H. Fjellvåg, Detailed electronic structure studies on superconducting MgB_2 and related compounds, Phys. Rev. B **64**, 224509 (2001).

[20] P. F. Karimov, N. A. Skorikov, E. Z. Kurmaev, L. D. Finkelstein, S. Leitch, J. MacNaughton, A. Moewes, and T. Mori, Resonant inelastic soft x-ray scattering and electronic structure of LiBC, J. Phys.: Condens. Matter **16**, 5137 (2004).

[21] H. Rosner, A. Kitaigorodsky, and W. E. Pickett, Prediction of high T_c superconductivity in hole-doped LiBC, Phys. Rev. Lett. **88**, 127001 (2002).

[22] J. K. Dewhurst, S. Sharma, C. Ambrosch-Draxl, and B. Johansson, First-principles calculation of superconductivity in hole-doped LiBC: $T_c = 65$ K, Phys. Rev. B **68**, 020504(R) (2003).

[23] A. M. Fogg, J. Meldrum, G. R. Darling, J. B. Claridge, and M. J. Rosseinsky, Chemical control of electronic structure and superconductivity in layered borides and borocarbides: Understanding the absence of superconductivity in Li_xBC, J. Am. Chem. Soc. **128**, 10043 (2006).

[24] A. Bharathi, S. J. Balaselvi, M. Premila, T. N. Sairam, G. L. N. Reddy, C. S. Sundar, and Y. Hariharan, Synthesis and search for superconductivity in LiBC, Solid State Commun. **124**, 423 (2002).

[25] D. Souptel, Z. Hossain, G. Behr, W. Löser, and C. Geibel, Synthesis and physical properties of LiBC intermetallics, Solid State Commun. **125**, 17 (2003).

[26] A. M. Fogg, P. R. Chalker, J. B. Claridge, G. R. Darling, and M. J. Rosseinsky, LiBC electronic, vibrational, structural, and low-temperature chemical behavior of a layered material isoelectronic with MgB_2, Phys. Rev. B **67**, 245106 (2003).

[27] R. Miao, J. Yang, M. Jiang, Q. L. Zhang, D. Cai, C. H. Fan, Z. Bai, C. C. Liu, F. P. Wu, and S. Y. Ma, First-principles study of superconductivity in the hole self-doped $LiB_{1.1}C_{0.9}$, J. Appl. Phys. **113**, 133910 (2013).

[28] Y. Quan and W. E. Pickett, $Li_{2x}BC_3$: Prediction of a second MgB_2-class high-temperature superconductor, Phys. Rev. B **102**, 144504 (2020).

[29] T. Bazhirov, Y. Sakai, S. Saito, and M. L. Cohen, Electron-phonon coupling and superconductivity in Li-intercalated layered borocarbide compounds, Phys. Rev. B **89**, 045136 (2014).

[30] V. Milashius, V. Pavlyuk, G. Dmytriv, and H. Ehrenberg, Phase equilibria and crystal structure relationships in the ternary Li–B–C system, Inorg. Chem. Front. **5**, 853 (2018).

[31] A. Noguchi, S. Emori, Y. Takahashi, K. Takase, T. Watanabe, K. Sekizawa, and Y. Takano, Synthesis and electrical and magnetic properties of $Li_xB_{1+y}C_{1-y}$, J. Phys.: Conf. Ser. **150**, 052188 (2009).

[32] A. Lazicki, C. S. Yoo, H. Cynn, W. J. Evans, W. E. Pickett, J. Olamit, K. Liu, and Y. Ohishi, Search for superconductivity in LiBC at high pressure: Diamond anvil cell experiments and first-principles calculations, Phys. Rev. B **75**, 054507 (2007).

[33] M. G. Zhang, The high-pressure semiconducting phase of LiBC, Europhys. Lett. **114**, 16001 (2016).

[34] M. Gao, X. W. Yan, Z. Y. Lu, and T. Xiang, Strong-coupling superconductivity in LiB_2C_2 trilayer films, Phys. Rev. B **101**, 094501 (2020).

[35] P. Modak, A. K. Verma, and A. K. Mishra, Prediction of superconductivity at 70 K in a pristine monolayer of LiBC, Phys. Rev. B **104**, 054504 (2021).

[36] N. W. Ashcroft, Metallic hydrogen: A high-temperature superconductor? Phys. Rev. Lett. **21**, 1748 (1968).

[37] P. Cudazzo, G. Profeta, A. Sanna, A. Floris, A. Continenza, S. Massidda, and E. K. U. Gross, *Ab initio* description of high-temperature superconductivity in dense molecular hydrogen, Phys. Rev. Lett. **100**, 257001 (2008).

[38] S. Azadi, B. Monserrat, W. M. C. Foulkes, and R. J. Needs, Dissociation of high-pressure solid molecular hydrogen: A quantum Monte Carlo and anharmonic vibrational study, Phys. Rev. Lett. **112**, 165501 (2014).

[39] J. McMinis, R. C. Clay, D. Lee, and M. A. Morales, Molecular to atomic phase transition in hydrogen under high pressure, Phys. Rev. Lett. **114**, 105305 (2015).

[40] J. Bekaert, M. Petrov, A. Aperis, P. M. Oppeneer, and M. V. Milošević, Hydrogen-induced high-temperature superconductivity in two-dimensional materials: The example of hydrogenated monolayer MgB_2, Phys. Rev. Lett. **123**, 077001 (2019).

[41] L. Yang, Y. P. Li, H. D. Liu, N. Jiao, M. Y. Ni, H. Y. Lu, P. Zhang, and C. S. Ting, Theoretical prediction of superconductivity in Boron Kagome monolayer: MB_3 (M = Be, Ca, Sr) and the hydrogenated CaB_3, Chin. Phys. Lett. **40**, 017402 (2023).

[42] P. F. Liu, F. P. Zheng, J. Y. Li, J. G. Si, L. M. Wei, J. R. Zhang, and B. T. Wang, Two-gap superconductivity in a Janus MoSH monolayer, Phys. Rev. B **105**, 245420 (2022).

[43] T. B. Rawal, L. H. Chang, H. D. Liu, H. Y. Lu, and C. S. Ting, Phonon-mediated superconductivity near the lattice instability in hole-doped hydrogenated monolayer hexagonal boron nitride, Phys. Rev. Mater. **6**, 054003 (2022).

[44] Y. P. Li, L. Yang, H. D. Liu, N. Jiao, M. Y. Ni, N. Hao, H. Y. Lu, and P. Zhang, Phonon-mediated superconductivity in two-dimensional hydrogenated phosphorus carbide: HPC_3, Phys. Chem. Chem. Phys. **24**, 9256 (2022).

[45] Y. L. Han, Y. P. Li, L. Yang, H. D. Liu, N. Jiao, B. T. Wang, H. Y. Lu, and P. Zhang, High-temperature superconductivity in two-dimensional hydrogenated titanium diboride: $Ti_2B_2H_4$, Mater. Today Phys. **30**, 100954 (2023).

[46] Y. L. Xi, X. L. Jing, Z. F. Xu, N. N. Liu, Y. N. Liu, M. L. Lin, M. Yang, Y. Sun, J. C. Zhuang, X. Xu, W. C. Hao, Y. C. Li, X. D. Li, X. J. Wei, P. H. Tan, Q. J. Li, B. B. Liu, S. X. Dou, and Y. Du, Superconductivity in layered van der Waals hydrogenated germanene at high pressure, J. Am. Chem. Soc. **144**, 18887 (2022).

[47] J. Bekaert, C. Sevik, and M. V. Milošević, Enhancing superconductivity in MXenes through hydrogenation, Nanoscale **14**, 9918 (2022).

[48] J. Bekaert, A. Aperis, B. Partoens, P. M. Oppeneer, and M. V. Milošević, Evolution of multigap superconductivity in the atomically thin limit: Strain-enhanced three-gap superconductivity in monolayer MgB_2, Phys. Rev. B **96**, 094510 (2017).

[49] L. L. Liu, X. H. Liu, P. Song, L. Y. Zhang, X. W. Huang, W. F. Zhang, Z. Y. Zhang, and Y. Jia, Surface superconductivity with high transition temperatures in layered $Ca_nB_{n+1}C_{n+1}$ films, Nano Lett. **23**, 1924 (2023).

[50] P. Giannozzi, S. Baroni, N. Bonini, M. Calandra, R. Car, C. Cavazzoni, D. Ceresoli, G. L. Chiarotti, M. Cococcioni, I. Dabo, A. D. Corso, S. de Gironcoli, S. Fabris, G. Fratesi, R. Gebauer, U. Gerstmann, C. Gougoussis, A. Kokalj, M. Lazzeri, L. Martin-Samos *et al.*, QUANTUM ESPRESSO: A modular and open-source software project for quantum simulations of materials, J. Phys.: Condens. Matter **21**, 395502 (2009).

[51] G. Kresse and J. Hafner, *Ab initio* molecular dynamics for open-shell transition metals, Phys. Rev. B **48**, 13115 (1993).

[52] P. E. Blöchl, Projector augmented-wave method, Phys. Rev. B **50**, 17953 (1994).

[53] G. Kresse and J. Furthmüller, Efficiency of *ab-initio* total energy calculations for metals and semiconductors using a plane-wave basis set, Comput. Mater. Sci. **6**, 15 (1996).

[54] J. P. Perdew, K. Burke, and M. Ernzerhof, Generalized gradient approximation made simple, Phys. Rev. Lett. **77**, 3865 (1996).

[55] M. Methfessel and A. T. Paxton, High-precision sampling for Brillouin-zone integration in metals, Phys. Rev. B **40**, 3616 (1989).

[56] S. Baroni, S. de Gironcoli, A. D. Corso, and P. Giannozzi, Phonons and related crystal properties from density-functional perturbation theory, Rev. Mod. Phys. **73**, 515 (2001).

[57] N. Marzari and D. Vanderbilt, Maximally localized generalized Wannier functions for composite energy bands, Phys. Rev. B **56**, 12847 (1997).

[58] I. Souza, N. Marzari, and D. Vanderbilt, Maximally localized Wannier functions for entangled energy bands, Phys. Rev. B **65**, 035109 (2001).

[59] A. A. Mostofi, J. R. Yates, Y. S. Lee, I. Souza, D. Vanderbilt, and N. Marzari, wannier90: A tool for obtaining maximally-localised Wannier functions, Comput. Phys. Commun. **178**, 685 (2008).

[60] F. Giustino, M. L. Cohen, and S. G. Louie, Electron-phonon interaction using Wannier functions, Phys. Rev. B **76**, 165108 (2007).

[61] J. Noffsinger, F. Giustino, B. D. Malone, C. H. Park, S. G. Louie, and M. L. Cohen, EPW: A program for calculating the electron–phonon coupling using maximally localized Wannier functions, Comput. Phys. Commun. **181**, 2140 (2010).

[62] E. R. Margine and F. Giustino, Anisotropic Migdal-Eliashberg theory using Wannier functions, Phys. Rev. B **87**, 024505 (2013).

[63] Y. Zhao, C. Lian, S. Zeng, Z. Dai, S. Meng, and J. Ni, MgB_4 trilayer film: A four-gap superconductor, Phys. Rev. B **101**, 104507 (2020).

[64] Y. Zhao, C. Lian, S. Zeng, Z. Dai, S. Meng, and J. Ni, Two-gap and three-gap superconductivity in AlB_2-based films, Phys. Rev. B **100**, 094516 (2019).

[65] J. Kortus, I. I. Mazin, K. D. Belashchenko, V. P. Antropov, and L. L. Boyer, Superconductivity of metallic boron in MgB_2, Phys. Rev. Lett. **86**, 4656 (2001).

[66] T. Yildirim, O. Gülseren, J. W. Lynn, C. M. Brown, T. J. Udovic, Q. Huang, N. Rogado, K. A. Regan, M. A. Hayward, J. S. Slusky, T. He, M. K. Haas, P. Khalifah, K. Inumaru, and R. J. Cava, Giant anharmonicity and nonlinear electron-phonon coupling in MgB_2: A combined first-principles calculation and neutron scattering study, Phys. Rev. Lett. **87**, 037001 (2001).

[67] A. Migdal, Interaction between electrons and lattice vibrations in a normal metal, Sov. Phys. JETP **7**, 996 (1958).

[68] G. Eliashberg, Interactions between electrons and lattice vibrations in a superconductor, Sov. Phys. JETP **11**, 696 (1960).

[69] P. B. Allen and B. Mitrović, *Theory of Superconducting T_c* (Academic Press, New York, 1983), pp. 1–92.

[70] F. Marsiglio, M. Schossmann, and J. P. Carbotte, Iterative analytic continuation of the electron self-energy to the real axis, Phys. Rev. B **37**, 4965 (1988).

[71] W. Kohn, Image of the fermi surface in the vibration spectrum of a metal, Phys. Rev. Lett. **2**, 393 (1959).

[72] Z. C. Wang, S. M. Zeng, Y. C. Zhao, X. M. Wang, and J. Ni, Three-gap superconductivity in two-dimensional InB_2/InB_4 films, Phys. Rev. B **104**, 174519 (2021).

[73] F. Giustino, Electron-phonon interactions from first principles, Rev. Mod. Phys. **89**, 015003 (2017).

[74] Y. L. Hai, M. J. Jiang, H. L. Tian, G. H. Zhong, W. J. Li, C. L. Yang, X. J. Chen, and H. Q. Lin, Superconductivity above 100 K predicted in carbon-cage network, Adv. Sci. **10**, 2303639 (2023).

[75] C. Si, Z. Liu, W. H. Duan, and F. Liu, First-principles calculations on the effect of doping and biaxial tensile strain on electron-phonon coupling in graphene, Phys. Rev. Lett. **111**, 196802 (2013).

[76] G. Savini, A. C. Ferrari, and F. Giustino, First-principles prediction of doped graphane as a high-temperature electron-phonon superconductor, Phys. Rev. Lett. **105**, 037002 (2010).

[77] A. Floris, G. Profeta, N. N. Lathiotakis, M. Lüders, M. A. L. Marques, C. Franchini, E. K. U. Gross, A. Continenza, and S. Massidda, Superconducting properties of MgB_2 from first principles, Phys. Rev. Lett. **94**, 037004 (2005).

[78] A. Floris, A. Sanna, S. Massidda, and E. K. U. Gross, Two-band superconductivity in Pb from *ab initio* calculations, Phys. Rev. B **75**, 054508 (2007).

[79] T. T. Gai, P. J. Guo, H. C. Yang, Y. Gao, M. Gao, and Z. Y. Lu, Van Hove singularity induced phonon-mediated superconductivity above 77 K in hole-doped SrB_3C_3, Phys. Rev. B **105**, 224514 (2022).

[80] K.-H. Lee, K. J. Chang, and M. L. Cohen, First-principles calculations of the Coulomb pseudopotential μ^*: Application to Al, Phys. Rev. B **52**, 1425 (1995).

[81] C. F. Richardson and N. W. Ashcroft, High temperature superconductivity in metallic hydrogen: Electron-electron enhancements, Phys. Rev. Lett. **78**, 118 (1997).

[82] N. N. Hieu, H. V. Phuc, A. I. Kartamyshev, and T. V. Vu, Structural, electronic, and transport properties of quintuple atomic Janus monolayers Ga_2SX_2 (X = O, S, Se, Te): First-principles predictions, Phys. Rev. B **105**, 075402 (2022).

[83] C. Ataca, M. Topsakal, E. Aktürk, and S. Ciraci, A comparative study of lattice dynamics of three- and two-dimensional MoS_2, J. Phys. Chem. C **115**, 16354 (2011).

[84] A. Fleurence, R. Friedlein, T. Ozaki, H. Kawai, Y. Wang, and Y. Yamada-Takamura, Experimental evidence for epitaxial silicene on diboride thin films, Phys. Rev. Lett. **108**, 245501 (2012).

[85] J. P. Ji, X. F. Song, J. Z. Liu, Z. Yan, C. X. Huo, S. L. Zhang, M. Su, L. Liao, W. H. Wang, Z. H. Ni, Y. F. Hao, and H. B. Zeng, Two-dimensional antimonene single crystals grown by van der Waals epitaxy, Nat. Commun. **7**, 13352 (2016).

[86] L. K. Li, Y. J. Yu, G. J. Ye, Q. Q. Ge, X. D. Ou, H. Wu, D. L. Feng, X. H. Chen, and Y. B. Zhang, Black phosphorus field-effect transistors, Nat. Nanotechnol. **9**, 372 (2014).

[87] H. T. Yuan, X. G. Liu, F. Afshinmanesh, W. Li, G. Xu, J. Sun, B. Lian, A. G. Curto, G. J. Ye, Y. Hikita, Z. X. Shen, S. C. Zhang, X. H. Chen, M. Brongersma, H. Y. Hwang, and Y. Cui, Polarization-sensitive broadband photodetector using a black phosphorus vertical p–n junction, Nat. Nanotechnol. **10**, 707 (2015).

[88] B. J. Feng, B. T. Fu, S. Kasamatsu, S. Ito, P. Cheng, C. C. Liu, Y. Feng, S. L. Wu, S. K. Mahatha, P. Sheverdyaeva, P. Moras, M. Arita, O. Sugino, T. C. Chiang, K. Shimada, K. Miyamoto, T. Okuda, K. H. Wu, L. Chen, Y. G. Yao, and I. Matsuda, Experimental realization of two-dimensional Dirac nodal line fermions in monolayer Cu_2Si, Nat. Commun. **8**, 1007 (2017).

[89] M. Pumera and Z. Sofer, 2D monoelemental arsenene, Antimonene, and Bismuthene: Beyond black Phosphorus, Adv. Mater. **29**, 1605299 (2017).

[90] C. F. Fu, J. Y. Sun, Q. Q. Luo, X. X. Li, W. Hu, and J. L. Yang, Intrinsic electric fields in two-dimensional materials boost the solar-to-hydrogen efficiency for photocatalytic water splitting, Nano Lett. **18**, 6312 (2018).

[91] J. D. Zhou, Q. S. Zeng, D. H. Lv, L. F. Sun, L. Niu, W. Fu, F. C. Liu, Z. X. Shen, C. H. Jin, and Z. Liu, Controlled synthesis of high-quality monolayered α-In_2Se_3 via physical vapor deposition, Nano Lett. **15**, 6400 (2015).

[92] G. Almeida, S. Dogan, G. Bertoni, C. Giannini, R. Gaspari, S. Perissinotto, R. Krahne, S. Ghosh, and L. Manna, Colloidal monolayer β-In_2Se_3 nanosheets with high photoresponsivity, J. Am. Chem. Soc. **139**, 3005 (2017).

[93] F. Reis, G. Li, L. Dudy, M. Bauernfeind, S. Glass, W. Hanke, R. Thomale, J. Schäfer, and R. Claessen, Bismuthene on a SiC substrate: A candidate for a high-temperature quantum spin Hall material, Science **357**, 287 (2017).

[94] H. K. Mao, A. P. Jephcoat, R. J. Hemley, L. W. Finger, C. S. Zha, R. M. Hazen, and D. E. Cox, Synchrotron X-ray diffraction measurements of single-crystal hydrogen to 26.5 gigapascals, Science **239**, 1131 (1988).

[95] A. W. Overhauser, Crystal structure of lithium at 4.2 K, Phys. Rev. Lett. **53**, 64 (1984).

[96] K. Lejaeghere, V. Van Speybroeck, G. V. Oost, and S. Cottenier, Error estimates for solid-state density-functional theory predictions: An overview by means of the ground-state elemental crystals, Crit. Rev. Solid State Mater. Sci. **39**, 1 (2014).

[97] G. Will and B. Kiefer, Electron deformation density in rhombohedral α-boron, Z. Anorg. Allg. Chem. **627**, 2100 (2001).

[98] G. Parakhonskiy, N. Dubrovinskaia, L. Dubrovinsky, S. Mondal, and S. van Smaalen, High pressure synthesis of single crystals of α-boron, J. Cryst. Growth **321**, 162 (2011).

[99] A. R. Ubbelohde, G. S. Parry, and D. Nixon, Order–disorder transformations in graphite nitrates, Nature (London) **206**, 1352 (1965).

[100] R. C. Andrew, R. E. Mapasha, A. M. Ukpong, and N. Chetty, Mechanical properties of graphene and boronitrene, Phys. Rev. B **85**, 125428 (2012).

[101] W. Z. Xiao, G. Xiao, and L. L. Wang, A first-principles study of the SnO_2 monolayer with hexagonal structure, J. Chem. Phys. **145**, 174702 (2016).

[102] Y. Guo, S. Zhou, Y. Bai, and J. Zhao, Enhanced piezoelectric effect in Janus group-III chalcogenide monolayers, Appl. Phys. Lett. **110**, 163102 (2017).

[103] C. S. Liu, H. H. Zhu, X. J. Ye, and X. H. Yan, Prediction of a new BeC monolayer with perfectly planar tetracoordinate carbons, Nanoscale **9**, 5854 (2017).

[104] R. C. Cooper, C. Lee, C. A. Marianetti, X. Wei, J. Hone, and J. W. Kysar, Nonlinear elastic behavior of two-dimensional molybdenum disulfide, Phys. Rev. B **87**, 035423 (2013).

[105] D. G. Papageorgiou, I. A. Kinloch, and R. J. Young, Mechanical properties of graphene and graphene-based nanocomposites, Prog. Mater. Sci. **90**, 75 (2017).

[106] E. Cadelano, P. L. Palla, S. Giordano, and L. Colombo, Elastic properties of hydrogenated graphene, Phys. Rev. B **82**, 235414 (2010).

[107] T. V. Vu, V. T. T. Vi, H. V. Phuc, A. I. Kartamyshev, and N. N. Hieu, Oxygenation of Janus group III monochalcogenides: First-principles insights into GaInXO (X = S, Se, Te) monolayers, Phys. Rev. B **104**, 115410 (2021).

[108] T. N. Do, N. N. Hieu, N. A. Poklonski, N. T. T. Binh, C. Q. Nguyen, and N. D. Hien, Computational insights into structural, electronic, and optical properties of Janus GeSO monolayer, RSC Adv. **11**, 28381 (2021).

[109] S. D. Guo, X. S. Guo, R. Y. Han, and Y. Deng, Predicted Janus SnSSe monolayer: A comprehensive first-principles study, Phys. Chem. Chem. Phys. **21**, 24620 (2019).

[110] G. Kresse and J. Furthmüller, Efficient iterative schemes for *ab initio* total-energy calculations using a plane-wave basis set, Phys. Rev. B **54**, 11169 (1996).

[111] M. Calandra and F. Mauri, Charge-density wave and superconducting dome in $TiSe_2$ from electron-phonon interaction, Phys. Rev. Lett. **106**, 196406 (2011).

[112] H. L. Zhuang, M. D. Johannes, A. K. Singh, and R. G. Hennig, Doping-controlled phase transitions in single-layer MoS_2, Phys. Rev. B **96**, 165305 (2017).

[113] J. G. Si, W. J. Lu, H. Y. Wu, H. Y. Lv, X. Liang, Q. J. Li, and Y. P. Sun, Origin of the multiple charge density wave order in $1T - VSe_2$, Phys. Rev. B **101**, 235405 (2020).

[114] G. Henkelman, A. Arnaldsson, and H. Jonsson, A fast and robust algorithm for Bader decomposition of charge density, Comput. Mater. Sci. **36**, 354 (2006).